Letter of Intent for PAC 51

Measurement of
Double Deeply Virtual Compton Scattering in the di-muon channel with the SoLID spectrometer

Alexandre Camsonne*†, Kondo Gnanvo

Thomas Jefferson National Accelerator Facility
12000 Jefferson Avenue, Newport News, Virginia 23606, USA

Debaditya Biswas, Marie Boër*, Gyang Chung, Mahmoud Gomina

Virginia Tech
Virginia Polytechnic Institute and State University, Blacksburg, VA 24061

Gabriel Charles, Michel Guidal, Dominique Marchand, Carlos Muñoz Camacho, Silvia Niccolai, Eric Voutier*

Institut de Physique Nucléaire
IN2P3/CNRS, Université Paris Sud
15 rue Georges Clémenceau, 91406 Orsay, France

Zhiwen Zhao*

Duke University, Durham, NC 27708

Ronald Gilman

Rutgers University Rutgers, The State University of New Jersey
136 Frelinghuysen Road Piscataway, NJ 08854-8019

Nilanga Linayage

University of Virginia
Charlottesville, VA 22904-4714

Yi Wang, Junhuai Xu, Zhihong Ye, Haojie Zhang, Yaopeng Zhang

Tsinghua University, Beijing 100084, China

Evaristo Cisbani

Istituto Superiore di Sanità
299 Viale Regina Elena, Roma 00161, Italia

Guido Maria Urcioli

INFN, Sezione di Roma1

2 Piazzale Aldo Moro, Roma 00185, Italia

Vincenzo Bellini, Concetta Maria Sutera

Dipartimento di Fisica a Astronomica, Università di Catania,
64 Via S. Sofia, Catania 95123, Italia

Anthony W. Thomas

ARC Special Research Centre for the Subatomic Structure of Matter (CSSM)
University of Adelaïde, School of Chemistry and Physics, Adelaïde SA 5005, Australia

Maxime Defurne, Hervé Moutarde, Franck Sabatié

DSM/IRFU/SPhN, CEA - Saclay
Bât. 141, Gif sur Yvette 91191, France

Malek Mazouz

Faculté des Sciences de Monastir, Département de Physique
Monastir 5000, Tunisia

Whitney Armstrong, Sylvester Joosten, Zein-Eddine Meziani

Argonne National Laboratory, Physics Division
Bdg. 203, 9700 S. Cass Avenue, Argonne IL 60439, USA

Thomas Hemmick

Stony Brook University, Department of Physics and Astronomy
C-107/S-200 Physics Building, Stony Brook NY 11794-3800, USA

and the Hall A SoLID collaboration

Proposal as of May 22, 2023

† Contact person
* Spokesperson

Executive Summary

This LOI is aiming at measuring Double Deeply Virtual Scattering (DDVCS) in the di-muons channel in parallel to the J/Ψ SoLID experiment (E12-12-006) by complementing it with a muon detector.

The main physics goal is to extract Compton Form Factors (CFFs) and Generalized Parton Distributions (GPDs) in regions where $x \neq \xi$ (respectively, longitudinal momentum fraction and skewness). Constraining the ξ dependence of the GPDs and deconvolute x and ξ, is essential to extrapolate the GPDs to $\xi = 0$ ("zero skewness" limit), for tomographic interpretations. Indeed, such interpretations rely on the Fourier Transform of GPDs at the limit $\xi = 0$, where one obtains x-dependent transverse partonic densities.

The measured observable will be the first ϕ-moment (angle between leptonic and hadronic plane) and φ_μ- moment (angle between the lepton pair and the hadronic plane) of the beam spin asymmetry which can be written [1]

$$\begin{Bmatrix} A_{\rm LU}^{\sin\phi} \\ A_{\rm LU}^{\sin\varphi_\mu} \end{Bmatrix} = \frac{1}{\mathcal{N}} \int_{\pi/4}^{3\pi/4} d\theta_\mu \int_0^{2\pi} d\varphi_\mu \int_0^{2\pi} d\phi \begin{Bmatrix} 2\sin\phi \\ 2\sin\varphi_\mu \end{Bmatrix} \frac{d^7\overrightarrow{\sigma} - d^7\overleftarrow{\sigma}}{dx_B\, dy\, dt\, d\phi\, dQ'^2\, d\Omega_\mu}$$
$$\propto \Im\mathrm{m}\left\{ F_1\mathcal{H} - \frac{t}{4M_N^2} F_2\mathcal{E} + \xi'(F_1+F_2)\widetilde{\mathcal{H}} \right\}, \quad (1)$$

with the normalization factor given by

$$\mathcal{N} = \int_{\pi/4}^{3\pi/4} d\theta_\mu \int_0^{2\pi} d\varphi_\mu \int_0^{2\pi} d\phi\, \frac{d^7\overrightarrow{\sigma} + d^7\overleftarrow{\sigma}}{dx_B\, dy\, dt\, d\phi\, dQ'^2\, d\Omega_\mu}, \quad (2)$$

and where we omit for clarity the (ξ', ξ, t)-dependence of the CFF. In the case of an unpolarized proton target, the measurement gives access to the out-of diagonal GPD H, i.e. at $x \neq \xi$ and $\xi' \neq \xi$.

The experimental requirements are the same as for the SoLID J/Ψ experiment. It will use the SoLID spectrometer with a 3μA electron beam on a 15 cm liquid hydrogen target for 50 days.

We are seeking feedback from the PAC. This is an update to LOI12-15-005 "Measurement of Double Deeply Virtual Compton Scattering (DDVCS) in the di-muon channel with the SoLID spectrometer", which was submitted to PAC43 in 2015.

A dedicated workshop on this physics was held in 2017 in Trento and this letter of intent benefits from its outcome [2] in particular [3][4] as well as further studies performed by the proponent, in particular a more realistic muon detector layout. The main difference with previous LOI is a focus on the parasitic measurement with J/Ψ with only a new forward muon detector.

Abstract

The Compton scattering of a virtual photon in the deep inelastic regime, or so-called Double Deeply Virtual Compton Scattering (DDVCS), constitutes a unique access to the generalized parton distributions (GPDs). The virtuality of the final photon allows to investigate in a decorrelated way the x- and ξ-dependences of the GPDs, as opposed to Deeply Virtual Compton Scattering accessing GPDs along the diagonals $x = \pm\xi$. This unique feature of DDVCS allows investigation of the ξ-dependence of GPDs which is of relevance, among others, for the determination of the transverse parton densities and the distribution of nuclear forces. Knowledge of GPD's ξ-dependence is essential for tomographic interpretations which rely on the extrapolation of the GPDs to "zero skewness" (i.e. $\xi = 0$ limit), to access momentum dependent transverse densities (Fourier transform of GPDs at $\xi = 0$). This letter proposes to investigate the DDVCS process $ep \to ep\gamma^*$ at 11 GeV incident beam energy in the di-muon channel ($ep\gamma^* \to ep\mu^+\mu^-$) with the SoLID spectrometer supplemented with muon detectors. The experimental run would be parallel to the SoLID J/Ψ experiment and would deliver a significant set of experimental data about di-muon production at different deep inelastic regimes, and would bring data for GPD physics at $Q^2 > Q'^2$ in a limited phase space region.

Contents

1 Introduction

The aim of this experiment is to advance our knowledge on the QCD matrix elements in electron-nucleon scattering reactions, giving us new insight on outstanding questions in nuclear physics, in particular the three-dimensional structure of the nucleon in terms of partonic constituents and tomographic interpretations. The nucleon structure in these reactions can be parameterized by matrix elements containing information about the position and/or momentum of the partons (quarks and gluons). The so-called Generalized Parton Distributions (GPDs) [5] profoundly renewed and extended the understanding of the structure and dynamics of the nucleon [6, 7]. GPDs contain information about the quarks and gluons transverse position versus their longitudinal momentum [8, 9]. Encoding the correlations between partons, GPDs access the internal dynamics of the nucleon as expressed by the Ji sum rule linking GPDs to the angular momentum [10], and the second moment of GPDs giving insights about the distribution of nuclear forces [11]. The first moment of GPDs link them to the electromagnetic Form Factors, while they take the form of parton distributions at their forward limit. Consequently, GPDs appear as fundamental building elements of the nuclear structure knowledge, asking for a precise and complete experimental determination.

We can access GPDs in reactions where all the products are known, as in elastic scattering (exclusive), and a highly virtual photon is exchanged off a quark, as in Deep Inelastic Scattering (DIS), providing a factorization scale [12] to separate the non-perturbative nucleon's structure part and a hard scattering part calculable in perturbative QCD. We will generically refer to Hard Exclusive Compton-like Scattering, which can be represented at leading order by the generic diagram 1. In this diagram, we included a dashed line to separate the hard pertubatively calculable part (coefficient function, on top), and the soft part where the parton's dynamic is parameterized by the GPDs (bottom part), in the QCD collinear factorization framework. We are using the incoming photon's virtuality (squared invariant mass $Q^2 = -q^2$) for factorization scale. In the case of Double Deeply Virtual Compton Scattering (DDVCS), the two photons are highly virtual, i.e. have a virtuality greater than 1 GeV^2, and are of different virtuality. The incoming photon (q) is spacelike, and the outgoing one (q') is virtual. Their virtualities are, respectively, $Q^2 = -q^2$ and $Q'^2 = +q'^2$. They enter in the evolution of the GPDs. Spacelike Deeply Virtual Compton Scattering (DVCS) and Timelike Compton Scattering (TCS) are the limit cases where, respectively, the outgoing, or incoming, photons are real. Besides the virtuality, only entering in evolution equations, the GPDs depend on 3 variables: the squared momentum transfer to the nucleon, $t = (p - p')^2$, which also contain the transverse component of the momentum transfer; the longitudinal momentum fraction x of the parton (as defined in DIS); and the skewness variable ξ, which is proportional to the longitudinal momentum transfer to the quark. The GPD's interpretation stand in the Bjorken regime where Q^2 (or Q'^2) is large ($\gg 1GeV^2$), and $t \to 0$. GPDs may be interpreted as a $1/Q$ resolution distribution in the transverse plane of partons carrying some longitudinal momentum fraction [13, 14, 15, 16, 17].

Hard Exclusive Compton-like Scattering reactions (DVCS, TCS, DDVCS...) are generally considered "golden channels" to access the GPDs, because the only non-perturbative part is the one parameterized by the GPDs, while other hard exclusive reactions may involve other parts such as the distribution amplitudes in hard exclusive meson production. DVCS has been experimentally studied for the past 20 years, first measurements of TCS where recently published by the CLAS12 Jlab Hall B collaboration [18]. While there are many advantages in studying DVCS and TCS to access GPDs, there are limitations to which kinematics can be accessed with these two processes. GPDs are accessed via the measurement of Compton Form Factors (CFFs), which are imaginary functions of GPDs where they enter in the forms of integrals over x. With DVCS and TCS, can extract the imaginary part involving GPDs at the $x = \pm\xi$ phase-space point while the real part is the convolution integral of GPDs and parton propagators over the whole physics range. In fine, DVCS and TCS allows to investigate unambiguously GPDs along the diagonals $x = \pm\xi$, but are therefore limited to a restricted region of the available phase space.

We can overcome this limitation with DDVCS thanks to the lever arm provided by the relative virtualities of the incoming and outgoing photons [19, 20, 3] and access the imaginary part of CFFs at $x \neq \xi$. Indeed, DDVCS access the GPDs in the so-called ERBL evolution region where $|x| \leq \xi$. It allows to decouple the experimental x- and ξ-dependences opening off-diagonal investigation of GPDs. More importantly, it enables

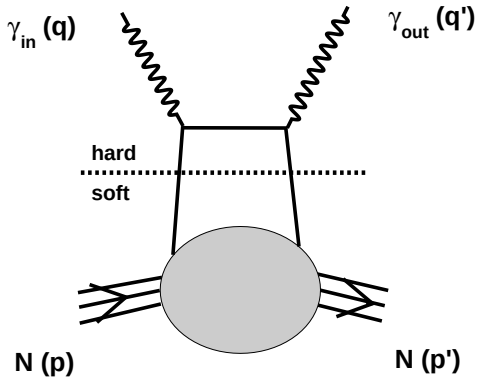

Figure 1: Generic diagram for Hard Exclusive Compton-like Scattering, where we represented the factorization line between the hard QCD-calculable part and the soft part parameterized by GPDs. Leading order and leading twist diagram.

to put constraints on the deconvolution of these two variables and the extrapolation of the skewness variable ξ to "zero momentum", which is needed for tomographic interpretations of the GPDs [13].

Taking advantage of the energy upgrade of the CEBAF accelerator and of the development of SoLID detection capabilities, this letter of intent propose to investigate the electroproduction of $\mu^+\mu^-$ di-muon pairs and measure the beam spin asymmetry of the exclusive $\vec{e}p \to ep\gamma^* \to ep\mu^+\mu^-$ reaction in the hard scattering regime. The reason for relying on the muon pairs decay channels rather than electrons is to prevent the complexification of the theoretical interpretations induced by the extra terms to antisymmetrize the wave functions (identical leptons), and the experimental difficulties and constraints of having a significant momentum gap between the 2 electrons to enable the reconstruction of the reaction's kinematics. For this reason, our analysis relies on the detection of muon pairs, and this letter of intent includes the addition of a muon detector behind the base SoLID spectrometer. We propose to take advantage of the luminosity capabilities of the SoLID spectrometer, and detecting the $\mu^+\mu^-$ di-muon pair from the virtual photon decay.

The next section reviews the main characteristics of the DDVCS process and the GPD content of the unpolarized cross section and beam spin asymmetry experimental observables. The benefits of DDVCS measurements for the achievement of the GPD experimental program are specifically discussed in the following section, before adressing the description of the experimental setup constituting of the base SoLID spectrometer and the forseen extension required for the di-muon detection. Finally, the expected counting rates and experimental data are presented based on the simulation package of the SoLID spectrometer and the VGG modeling [22] of the Bethe-Heitler and DDVCS cross sections.

2 Double deeply virtual Compton scattering Formalism

2.1 Electroproduction of photons

Similarly than the light diffusion from a material is telling about its internal structure, the light scattered by the nucleon carries information about the parton dynamics and organisation, providing that the wavelength associated to this light is smaller than the nucleon size. The Compton scattering of a virtual photon with quadri-momentum $Q^2 > 1$ $(\mathrm{GeV}/c^2)^2$ is capable of resolving the internal structure of the nucleon. The deep

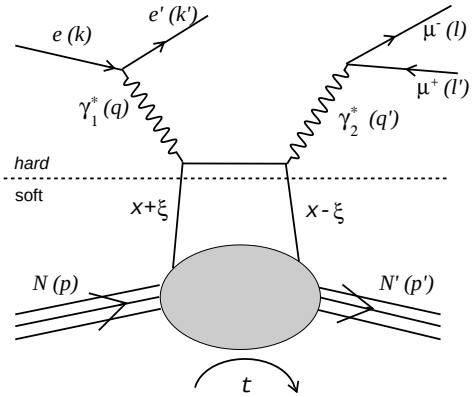

Figure 2: The handbag diagram, symbolizing also the DDVCS process: the initial and final virtual photon momenta are respectively q and q' and similarly the initial and final proton momenta are p and p'. Note: leading twist and leading order, CC diagram is not represented.

regime of this process, also known as double deeply virtual Compton scattering, is the simplest expression of the hanbag diagram (Fig. 2) allowing to access GPDs.

DDVCS is the most general case of the deeply virtual Compton scattering (DVCS) in which the initial virtual photon transforms into a real photon in the final state. DVCS has been the main focus of existing and developing experimental programs for the past 2 decades, since factorization was shown to hold already at electron beam energies of 6 GeV [23]. Several DVCS observables have been measured: polarized an unpolarized cross section off the proton [23, 24, 25, 26, 27, 28, 29, 30] and off the neutron [31, 32], beam spin asymmeties off the proton [33, 34, 35], target spin asymmetries off longitudinally [36, 37, 38, 39] and transversally [40] polarized protons, and beam charge asymmetries [41, 42].

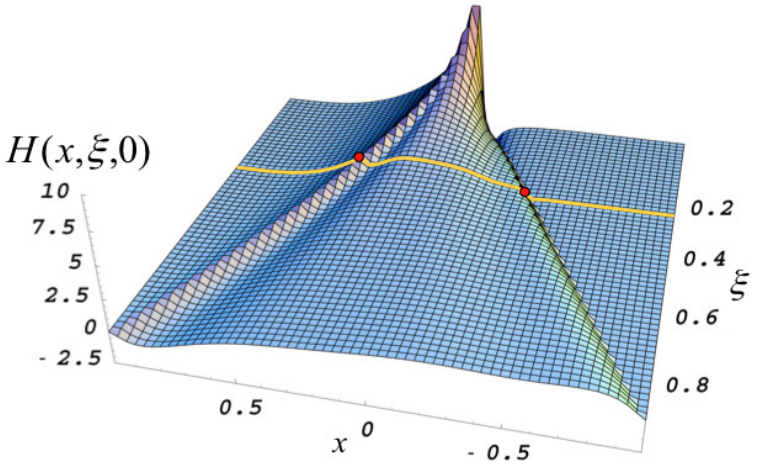

Figure 3: Graphical representation of the DVCS Compton form factor (CFF) showing a typical model for the GPD H at t=0; the red points indicates the GPD values involved in the CFF imaginary part, and the yellow line underlines the integral path of the CFF real part.

Physics understanding and detection techniques attached to DVCS experiments did reach very high scientific maturity which enables today the ability to take full advantage of the next experimental program

generation at JLab 12 GeV and COMPASS [43]. Future measurements of the DVCS process will allow for an unprecetended mapping of the nucleon GPDs via the separation of the Compton form factors (CFF), however limited to unambiguous interpretation only along specific correlation lines in the full GPDs kinematic phase-space.

2.2 Kinematics

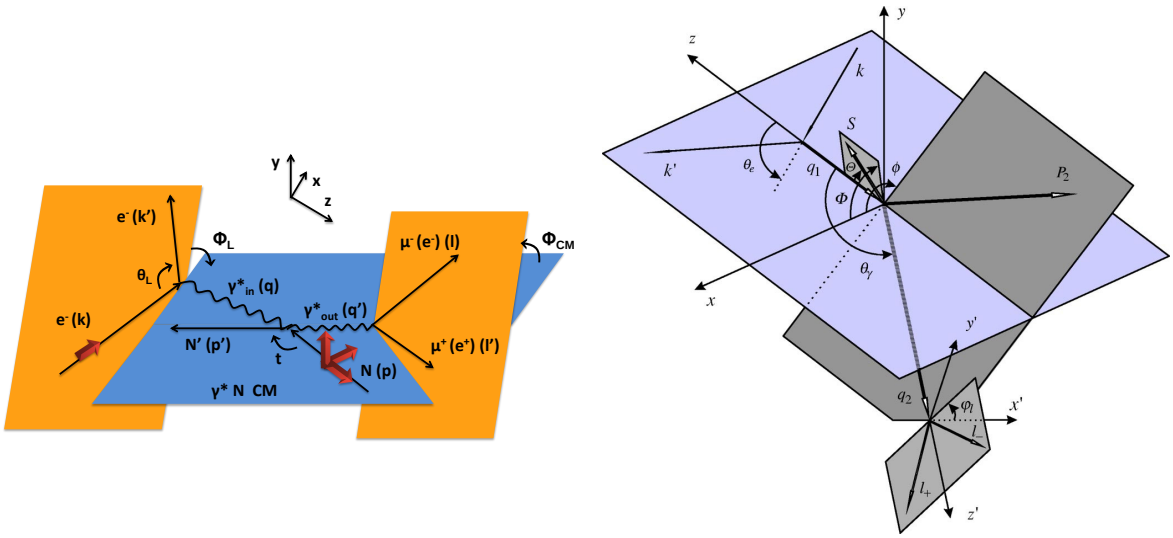

Figure 4: Reference frames for the DDVCS reaction, using notations defined in [19] (left) and in [20] (right).

We are using the notations defined in [19], expressed in the reference frames of Fig. 4 (left). The kinematics of the DDVCS in this frame using these nonations reads

$$e(k) - e'(k') + p(p_1) \equiv \gamma^\star(q_1) + p(p_1) \to p'(p_2) + \gamma^\star(q_2) \to p'(p_2) + \mu^+(l^+) + \mu^-(l^-), \tag{3}$$

where the photon virtualities are defined as

$$Q^2 = -q^2\,, \qquad Q'^2 = q'^2\,. \tag{4}$$

We define the symmetrical momentum variables p and q as

$$q = \frac{1}{2}(q + q')\,, \qquad p = p + p'\,, \tag{5}$$

and the four-momentum transfer to the nucleon $\Delta = p - p' = q - q'$ with $t = \Delta^2$, the DDVCS scaling variables write

$$x_B = -\frac{1}{2}\frac{q_1 \cdot q_1}{p_1 \cdot q_1}\,, \qquad \xi' = -\frac{q \cdot q}{p \cdot q}\,, \qquad \xi = \frac{\Delta \cdot q}{p \cdot q}\,. \tag{6}$$

The symmetrical momentum q can be decomposed as

$$q^2 = -\frac{1}{2}\left(Q^2 - Q'^2 + \frac{\Delta^2}{2}\right). \tag{7}$$

We can decompose the skewness variables in terms of virtualities and Δ:

$$\xi = \frac{Q^2 - Q'^2 + (\Delta^2/2)}{2(Q^2/x_B) - Q^2 - Q'^2 + \Delta^2}\,, \qquad \xi' = -\frac{Q^2 + Q'^2}{2(Q^2/x_B) - Q^2 - Q^{\text{`}2} + \Delta^2}\,, \tag{8}$$

which expresses GPDs variables of interest in terms of experimentally measured quantities. The different Q'^2-dependence in the numerators of ξ and ξ' expresses the ability to access out-of diagonals phase space,

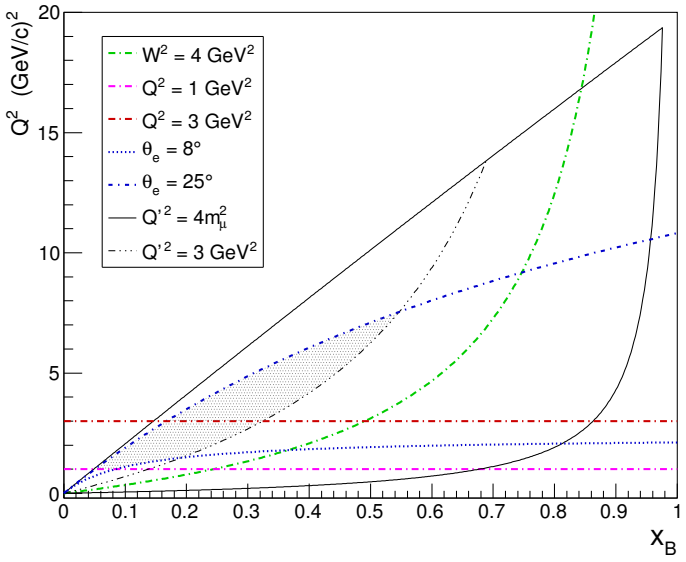

Figure 5: DDVCS experimental phase space for di-muon production at 11 GeV incident electron beam energy.

however limited by experimental and physics constraints. Note that for DVCS, $\xi = \xi'$, at the asymptotic limit.

The available experimental DDVCS phase space for di-muon production with an 11 GeV incident electron beam energy is represented on Fig. 5 in the (x_B, Q^2) plane: the inner space delimited by the full black lines corresponds to the kinematically allowed region; it is further restricted by the 1 GeV^2 lower Q^2-limit required at minima for the factorization of soft and hard scales, and the 4 GeV^2 lower W^2-limit insuring a deep inelastic process. Experimental constraints specific of the di-muon channel are expressed by the selection of the final virtual photon mass above 3 GeV^2 to minimize eventual contamination from vector mesons decay, leading to a minimum Q^2 (black dashed-line of Fig. 5). The SoLID spectrometer constraints is indicated by the blue lines corresponding to the 8°-25° angular coverage of the electron detector package. The combination of these different constraints yields the shaded area of Fig. 5. The additional red line separates the region $Q'^2 > Q^2$ (lower part) from the region $Q'^2 < Q^2$ (upper part), as a consequence of the minimum experimental Q'^2 requirement. The latter region is considered the domain of physics interest for applicability of the GPD formalism. Eq. 8 can be recast in

$$\xi' = \frac{x_B}{2 - x_B} \frac{1 - (Q'^2/Q^2) + (\Delta^2/2Q^2)}{1 - [x_B(Q'^2 - \Delta^2)/(2 - x_B)/Q^2]}, \qquad \xi = -\xi' \frac{1 + (Q'^2/Q^2)}{1 - (Q'^2/Q^2) + (\Delta^2/2Q^2)}, \tag{9}$$

showing that in the forward limit the DVCS process accesses the region $\xi{=}{-}\xi'$ ($\cong x_B/(2 - x_B)$), as noted previously. The (ξ', x_B) and (ξ', ξ) longitudinal momentum fraction phase space at Δ^2_{min} is shown on Fig. 6 for the SoLID experimental phase space indicated by the hatched area of Fig. 5. In both panels, the region delimited by the black lines corresponds to the full hatched area of Fig. 5 and the red area underlined the region $Q'^2 < Q^2$. The blue area corresponds to the DVCS phase space that would be covered under the same detection conditions but the maximum Q^2 restricted in this case by the condition $W > 2$ GeV/c^2; one notices that the Δ^2-dependence is responsible from small deviations from the $\xi{=}{-}\xi'$ line. In the most restricted case, the hyper-volume region corresponding to $x_B \in [0.17; 0.55]$, $Q^2 \in [3.0; 7.5]$, and $Q'^2 < Q^2$ would be explored, substanding the phase space $\xi' \in [-0.10; 0.21]$ and $\xi \in [-0.78; -0.20]$. Depending on true background conditions, one may access moderately larger phase space possibly extending up to the same W-limit as DVCS. The region $Q'^2 > Q^2$ would also allow to reach higher Q'^2, however within a different physics regime.

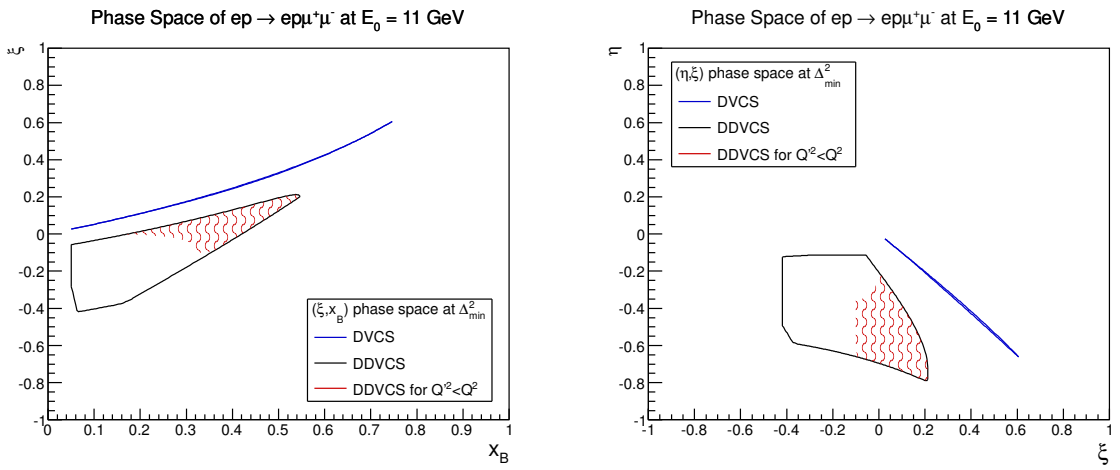

Figure 6: Longitudinal momentum fractions phase space for di-muon production at 11 GeV incident electron beam energy: (ξ, x_B) (left panel), and (ξ, ξ') (right panel). (note: in this figure, η stands for ξ and ξ stands for ξ')

2.3 Deconvolution of x and ξ and "off-diagonal" GPDs

The CFF $\mathcal{H}$ associated with the GPD H and accessible in DVCS polarized cross section or beam spin asymmetry experiments can be written

$$\mathcal{H}(\xi,t) = \sum_q e_q^2 \left\{ \mathcal{P} \int_{-1}^{1} dx\, H^q(x,\xi,t) \left[\frac{1}{\xi - x} - \frac{1}{\xi + x} \right] + i\pi \left[H^q(\xi,\xi,t) - H^q(-\xi,\xi,t) \right] \right\} \tag{10}$$

where the sum runs over all parton flavors with elementary electrical charge e_q, and $\mathcal{P}$ indicates the Cauchy principal value of the integral. While the imaginary part of the CFF accesses the GDP values at $x = \pm\xi$, it is clear from Eq. 10 that the real part of the CFF is a more complex quantity involving the convolution of parton propagators and the GPD values out-of the diagonals $x = \pm\xi$ (Fig. 3), that is in a domain that cannot be resolved unambiguously with DVCS experiments. Thanks to the virtuality of the final state photon, DDVCS provides a way to circumvent the DVCS limitation [19, 20], allowing to vary independently x and ξ. Considering the same GPD H, the corresponding CFF for the DDVCS process writes

$$\mathcal{H}(\xi',\xi,t) = \sum_q e_q^2 \left\{ \mathcal{P} \int_{-1}^{1} dx\, H^q(x,\xi,t) \left[\frac{1}{\xi' - x} - \frac{1}{\xi' + x} \right] + i\pi \left[H^q(\xi',\xi,t) - H^q(-\xi',\xi,t) \right] \right\} \tag{11}$$

involving the additional scaling variable ξ representing here the GPD skewness (Fig. 2). This variable obviously provides the necessary lever arm to investigate the GPD values out-of the diagonals (Fig. **??**), that is resolving part of the phase space of interest for the CFF real parts of both DVCS and DDVCS. The kinematically allowed phase space for out-of diagonal exploration is an increasing function of the beam energy but still remains significant at 11 GeV (Fig. 7).

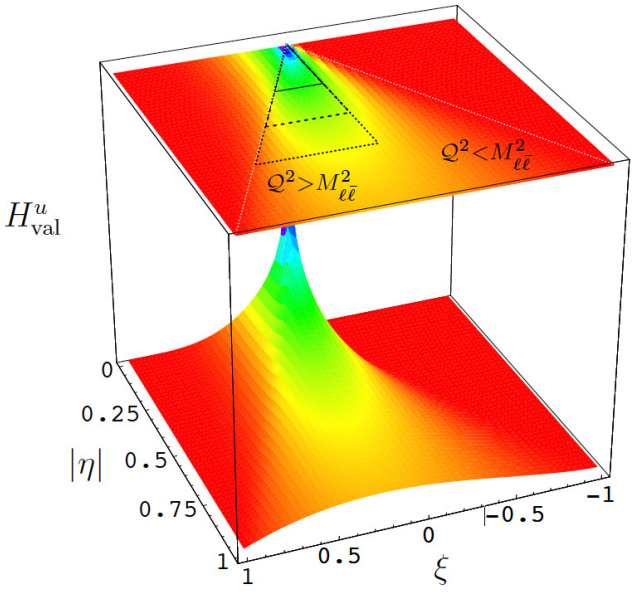

Figure 7: Example of coverage of the GPD surface for different electron beam energies and similar kinematic conditions [1]: 11 GeV (solid line), 25 GeV (dashed line), and 40 GeV (dotted line) in the GPD physics phase space $Q^2 > Q^{`2}$.

2.4 Unpolarized cross section

As the electroproduction of photons, di-muon electroproduction proceeds through the coherent sum of two essential processes: the DDVCS and the Bethe-Heitler (BH) mechanisms (Fig. 8). The latter process corresponds traditionally to the radiation of a photon by the incoming or outgoing electron (BH_1) before or after interacting elastically with the nucleon. In the case of di-muon electroproduction, another Bethe-Heitler like process occurs involving the virtual production of di-muons in the nuclear field (BH_2). Having the same final state, the cross section for the electroproduction of di-muons is built from the coherent interference of these processes. Depending on the incident beam energy the ratio of the DDVCS to BH contributions would change in favor of the DDVCS amplitude as the beam energy increases. The differential cross section for the electroproduction of di-muon off the nucleon may be written [1]

$$\frac{d^7\sigma}{dx_B\,dy\,dt\,d\phi\,dQ'^2\,d\Omega_\mu} = \frac{1}{(2\pi)^3}\,\frac{\alpha^4}{16}\,\frac{x_B y}{Q^2\sqrt{1+\varepsilon^2}}\,\sqrt{1-\frac{4m_\mu^2}{Q'^2}}\;|\mathcal{T}|^2, \tag{12}$$

where the reaction amplitude can generically be expressed as

$$|\mathcal{T}|^2 = |\mathcal{T}_{VCS}|^2 + \mathcal{I}_1 + \mathcal{I}_2 + |\mathcal{T}_{BH_1}|^2 + |\mathcal{T}_{BH_2}|^2 + \mathcal{T}_{BH_{12}}, \tag{13}$$

featuring the pure DDVCS amplitude $|\mathcal{T}_{VCS}|^2$, the interference amplitudes $\mathcal{I}_1$ and $\mathcal{I}_2$ between the DDVCS and Bethe-Heitler processes, and the pure BH amplitude built itself from the two elementary processes shown on Fig. 8. Following Ref. [1], the harmonic structure of the cross section writes

$$|\mathcal{T}_{VCS}|^2 = \frac{2\xi'^2}{Q^4 y^2 \tilde{y}^2(\xi^2-\xi'^2)} \quad \sum_{n=0}^{2} \left[c_n^{VCS}(\varphi_\mu)\cos(n\phi) + s_n^{VCS}(\varphi_\mu)\sin(n\phi)\right], \tag{14}$$

$$\mathcal{I}_1 = \frac{2\xi'(1-\xi)}{Q^2\Delta^2 y^3 \tilde{y}^3(\xi^2-\xi'^2)}\,\frac{\tilde{y}}{P_1P_2} \quad \sum_{n=0}^{3} \left[c_n^{1}(\varphi_\mu)\cos(n\phi) + s_n^{1}(\varphi_\mu)\sin(n\phi)\right], \tag{15}$$

$$\mathcal{I}_2 = \frac{2\xi'(1-\xi)}{Q^2\Delta^2 y^3 \tilde{y}^3(\xi^2-\xi'^2)}\,\frac{y}{P_3P_4} \quad \sum_{n=0}^{3} \left[c_n^{2}(\phi)\cos(n\varphi_\mu) + s_n^{2}(\phi)\sin(n\varphi_\mu)\right], \tag{16}$$

$$|\mathcal{T}_{BH_1}|^2 = -\frac{\xi'(1-\xi)^2}{Q^2\Delta^2 y^4 \tilde{y}^4 \xi(\xi^2-\xi'^2)}\left(\frac{\tilde{y}}{P_1P_2}\right)^2 \quad \sum_{n=0}^{4} \left[c_n^{11}(\varphi_\mu)\cos(n\phi) + s_n^{11}(\varphi_\mu)\sin(n\phi)\right], \tag{17}$$

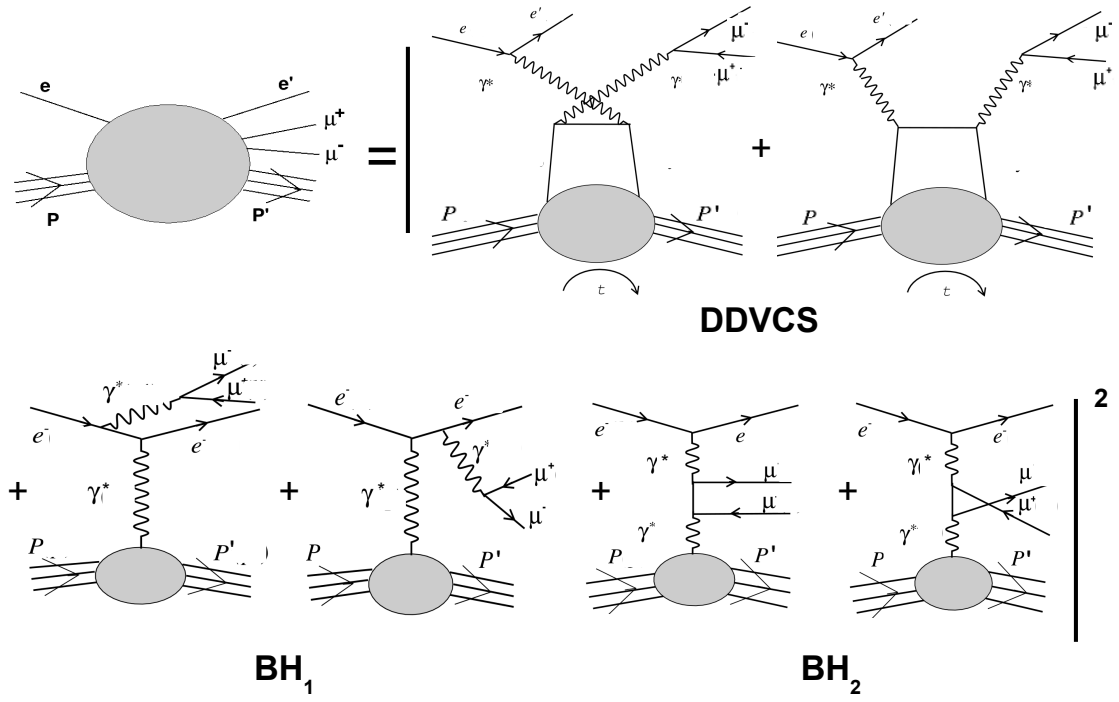

Figure 8: The different amplitudes contributing to the electroproduction of di-muons: the DDVCS, di-muon production from the initial and final leptons (BH_1), and the di-muon virtual production in the nuclear field (BH_2).

$$|\mathcal{T}_{BH_2}|^2 = -\frac{\xi'(1-\xi)^2}{Q^2\Delta^2 y^4\tilde{y}^4\xi(\xi^2-\xi'^2)}\left(\frac{y}{P_3P_4}\right)^2 \quad \sum_{n=0}^{4} \quad \left[c_n^{22}(\phi)\cos(n\varphi_\mu) + s_n^{22}(\phi)\sin(n\varphi_\mu)\right], \tag{18}$$

$$\mathcal{T}_{BH_{12}} = -\frac{\xi'(1-\xi)^2}{Q^2\Delta^2 y^4\tilde{y}^4\xi(\xi^2-\xi'^2)}\,\frac{y\tilde{y}}{P_1P_2P_3P_4} \quad \sum_{n=0}^{3} \quad \left[c_n^{12}(\varphi_\mu)\cos(n\phi) + s_n^{12}(\varphi_\mu)\sin(n\phi)\right], \tag{19}$$

where the P_i's correspond to the propagators of the intermediate leptons of the BH processes, and can be expressed as a function of the kinematics

$$P_1 = -\frac{1}{2\xi}\frac{(k'+\Delta)^2}{p\cdot q} \quad P_2 = -\frac{1}{2\xi}\frac{(k-\Delta)^2}{p\cdot q} \quad P_3 = \frac{1}{2\xi}\frac{(\mu_+ + \Delta)^2}{p\cdot q} \quad P_4 = \frac{1}{2\xi}\frac{(\mu_- + \Delta)^2}{p\cdot q}. \tag{20}$$

The Fourier coefficients read

$$c_n^i(\alpha) = \quad \sum_{m=0}^{2} \quad \left[cc_{nm}^i\cos(m\alpha) + cs_{nm}^i\sin(m\alpha)\right], \tag{21}$$

$$s_n^i(\alpha) = \quad \sum_{m=0}^{2} \quad \left[sc_{nm}^i\cos(m\alpha) + ss_{nm}^i\sin(m\alpha)\right], \tag{22}$$

for $i \equiv (VCS, 1, 2, 11, 12, 22)$ and $\alpha \equiv (\varphi_\mu, \phi)$, correspondingly. Similarly to the spacelike DVCS process, the $cc_{nm}^{VCS}, cs_{nm}^{VCS}, sc_{nm}^{VCS}, ss_{nm}^{VCS}$ coefficients are bi-linear combinations of Compton form factors, the coefficients for $i = 11, 12, 22$ are combinations of the nucleon electric and magnetic form factors, and the interference coefficients are linear combinations of the Compton form factors similar to the combinations measured in single DVCS. The full expression of the Fourier coefficients is lengthy detailed in Ref. [1]. It is worth noticing the symmetry properties of the BH propagators which obey

$$P_i(\phi) \quad = \quad P_i(2\pi - \phi), \tag{23}$$

$$P_j(\theta_\mu, \varphi_\mu) \quad = \quad P_j(\pi - \theta_\mu, \varphi_\mu + \pi), \tag{24}$$

for $i = \{1, 2, 3, 4\}$ and $j = \{3, 4\}$. As a consequence, the integration over $d\theta_\mu$ in a symmetric interval around θ_μ=$\pi/2$ for any definite moment in θ_μ reduces to a characteristic $\cos(k\varphi_\mu)$ Fourier expansion.

2.5 Beam spin asymmetry

The interference amplitude bewteen the BH and DDVCS processes is an observable of interest since it involves linear combinations of Compton form factors. The imaginary part can be accessed in via beam spin asymmetries. Considering the harmonic dependence of the cross section, it was shown [1] that the same basic information about GPDs can be obtained from the appropriate moments in ϕ or φ_μ, a feature of particular interest for experimental consistency. Taking advantage of the symmetry properties of the BH propagators to minimize the BH contribution, the first ϕ-moment and φ_μ-moment of the beam spin asymmetry can be written [1]

$$\begin{aligned}
\left\{ \begin{array}{c} A_{\rm LU}^{\sin\phi} \\ A_{\rm LU}^{\sin\varphi_\mu} \end{array} \right\} \quad &= \quad \frac{1}{\mathcal{N}} \int_{\pi/4}^{3\pi/4} d\theta_\mu \int_0^{2\pi} d\varphi_\mu \int_0^{2\pi} d\phi \left\{ \begin{array}{c} 2\sin\phi \\ 2\sin\varphi_\mu \end{array} \right\} \frac{d^7\overrightarrow{\sigma} - d^7\overleftarrow{\sigma}}{dx_B\, dy\, dt\, d\phi\, dQ'^2\, d\Omega_\mu} \\
&\propto \Im\mathrm{m} \left\{ F_1\mathcal{H} - \frac{t}{4M_N^2} F_2\mathcal{E} + \xi'(F_1 + F_2)\widetilde{\mathcal{H}} \right\}, \qquad (25)
\end{aligned}$$

with the normalization factor given by

$$\mathcal{N} = \int_{\pi/4}^{3\pi/4} d\theta_\mu \int_0^{2\pi} d\varphi_\mu \int_0^{2\pi} d\phi \, \frac{d^7\overrightarrow{\sigma} + d^7\overleftarrow{\sigma}}{dx_B\, dy\, dt\, d\phi\, dQ'^2\, d\Omega_\mu}, \tag{26}$$

and where we omit for clarity the (ξ', ξ, t)-dependence of the CFF. In the case of a proton target the measurement gives access to the out-of diagonal GPD H.

2.6 Theoretical projections

Fig. 9 displays the differential cross section and the beam spin asymmetry A_{LU} from the VGG model [22] for the di-muon production process at two relevant kinematics for the determination of GPDs. These experimental observables have been obtained using the prescription of Eq. 32 for the integration over the angular phase space of the di-muon pair. Sizeable asymmetries are predicted together with, as expected, a strong sensitivity of the cross section to kinematic conditions.

Because of the strong correlation between the azimuthal and polar angle of the final muon pair, we also provided calculations at different values of ϕ_μ and θ_μ for the unpolarized cross section (Fig. 10) and beam spin asymmetry (Fig. 11). The actual observables that will be used for the extraction of the CFFs are unpolarized cross sections and beam spin asymmetries differential in the initial and final azimuthal angles, integrated over the final polar angle. Extremes values in θ are cut out from this integral ($40 \leq \theta_\mu \leq 140^0$), due to the large BH dominance in this regions coming from the peaks induced by the "BH2" diagrams as illustrated Fig 8.

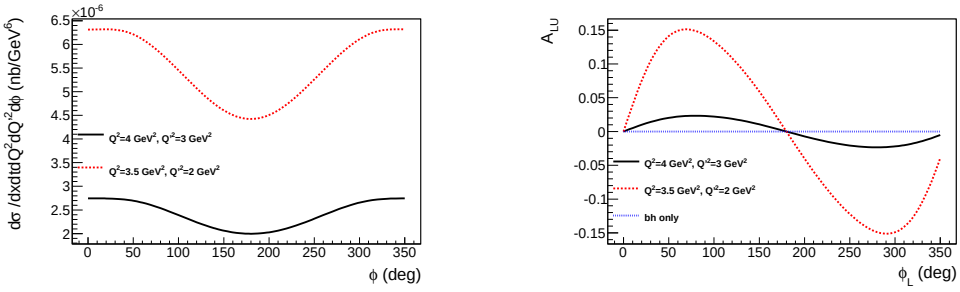

Figure 9: Out-of-plane angular dependence of the differential cross section (left) and the beam spin asymmetry (right) for the ^{1}H$(e, e'p\mu^+\mu^-)$ process at E=11 GeV, x_B=0.25, t=-0.4 GeV^2, and different virtual photon masses.

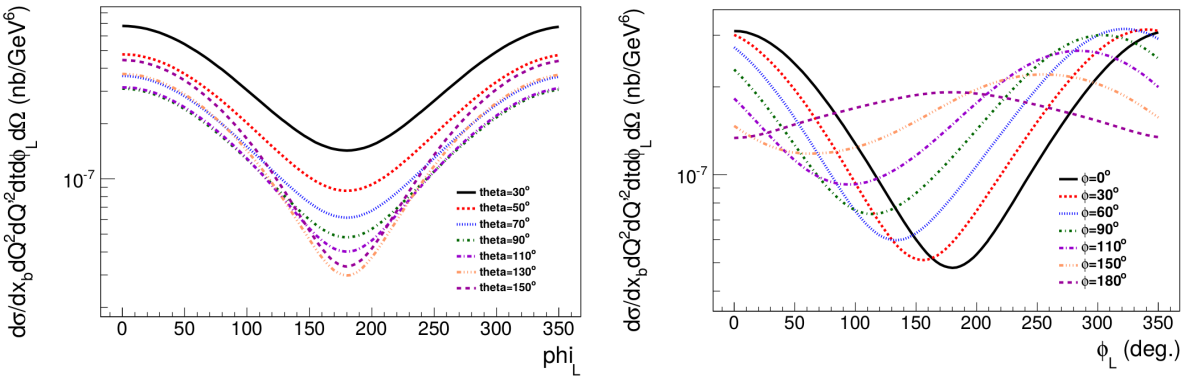

Figure 10: Out-of-plane angular dependence of the differential cross section for various polar angles of the muon (left) and various azimuthal angles of the muon (right).

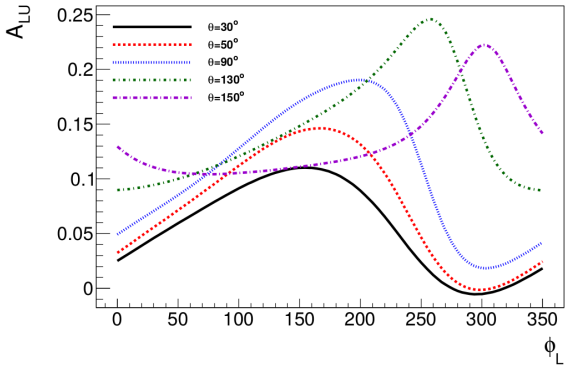

Figure 11: Out-of-plane angular dependence of the differential beam spin asymmetry for various polar angles of the muon.

3 Motivations and DDVCS benefits for the GPD program

3.1 GPDs at zero skewness, tomography of the nucleon

GPDs provide new visual insight on the partonic structure of matter by allowing for a tomography of the nucleon [13, 15]. In the particular case of zero skewdness, GPDs acquire a well-defined probability interpretation in the infinite momentum frame, similarly to conventional parton distributions. Indeed, the impact parameter dependent parton distribution related to H^q can be written [46]

$$q(x, \mathbf{b}_\perp) = \frac{1}{(2\pi)^2} \int d^2\mathbf{\Delta}_\perp \, H^q(x, 0, -\mathbf{\Delta}_\perp^2) \, e^{-i\mathbf{b}_\perp \cdot \mathbf{\Delta}_\perp} \tag{27}$$

telling that $q(x, \mathbf{b}_\perp)$ is the Fourier transform of $H^q(x, 0, -\mathbf{\Delta}_\perp^2)$. Therefore, the knowledge of GPDs at zero skewdness allows to determine the probability to find a parton carrying the light-cone longitudinal momentum fraction x of the nucleon at a transverse distance $\mathbf{b}_\perp$ from the center of momentum. Since they are linked to form factors through the 0^{th}-order Mellin moment, GPDs can also be seen as a light-cone momentum decomposition of form factors. As of today, access to zero skewdness GPDs for any momentum fraction x is only obtained from a (strongly underconstrained) model dependent interpretation of current DVCS data allowing for ξ-dependence extrapolation. Bringing uncorrelated information on the ξ-dependence of GPDs, DDVCS will ultimately allow for a model-independent interpretation of data providing a truly experimental determination of the parton transverse densities. An illustration of a momentum dependent impact parameter parton distribution function of GPD H is presented Fig 12.

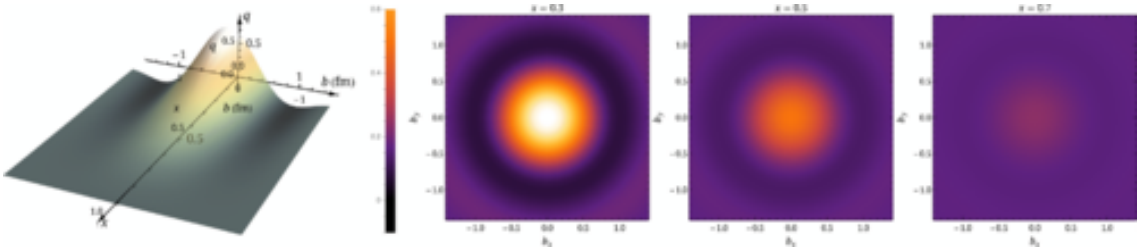

Figure 12: (Left) 3-dimensional momentum dependent impact parameter parton distribution function of GPD H, from lattice calculations at physical pion mass. (Right) Projection at x=.3, .5, .7, 2 dimensional impact parameter dependent function (From [47])

3.2 GPDs in the ERBL region

The partonic interpretation of GPDs in the region accessible to DDVCS, was introduced by M. Diehl in [8] and describes the virtual photon- quark interaction in the ERBL (Efremov–Radyushkin–Brodsky–Lepage) region as the exchange of a quark-antiquark pair (Fig. 13. There is currently no constrain on GPDs in this region, thus any measurement will enable us to learn about the probability of probing quark-antiquark pairs in the nucleon and putting constraints in this region.

3.3 Other interpretations

Additionally, the ξ-dependence of GPDs contains unique information about the distribution of nuclear forces. Polynomiality is a major property of GPDs which expresses that the n^{th} order Mellin moment of a GPD is a polynomial in ξ of maximal $(n+1)^{\text{th}}$ order [10]

$$\int_{-1}^{1} dx \, x^n \sum_q H^q(x, \xi, t) = \sum_{i=0}^{n+1} \sum_q h_i^{q(n)}(t) \, \xi^n \, . \tag{28}$$

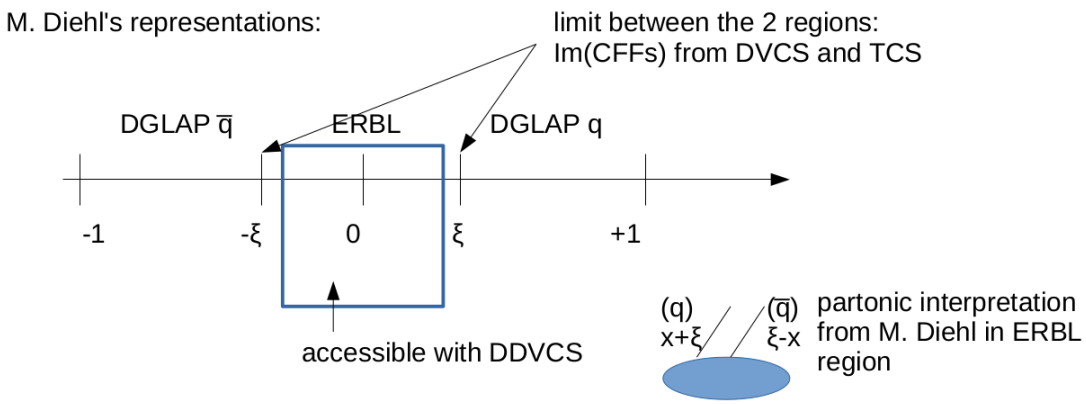

Figure 13: Partonic interpretation of the GPDs in the ERBL region, accessible with DDVCS (inspired by M. Diehl diagrams).

Following time reversal invariance, the polynomial expansion contains only even power of ξ [45], such that for instance

$$\int_{-1}^{1} dx\, x \sum_q H^q(x,\xi,t) = \sum_q h_0^{q(1)}(t) + \sum_q h_2^{q(1)}(t)\,\xi^2\,. \tag{29}$$

Futhermore, because on the spin 1/2 of the nucleon, the coefficient of the highest power in ξ for the GPDs H^q and E^q are related [45], leading to

$$\int_{-1}^{1} dx\, x \sum_q E^q(x,\xi,t) = \sum_q e_0^{q(1)}(t) - \sum_q h_2^{q(1)}(t)\,\xi^2\,, \tag{30}$$

consistently with the ξ-independence of the Ji sum rule [6]. Within the double distribution ansatz, the coefficient of the highest power in ξ is related to the so-called D-term which described GPDs out-of the diagonals $x = \pm\xi$ and therefore enters the real part of the corresponding DVCS CFF. The first Mellin moment of the H GPD can be recast

$$\int_{-1}^{1} dx\, x \sum_q H^q(x,\xi,t) = \sum_q M_2^q(t) + \frac{4}{5}\sum_q d_1^q(t)\,\xi^2, \tag{31}$$

where $d_1^q(t)$ is the first coefficient of the Gengenbauer expansion of the D-term [48]. In the forward limit, the first term of the right-hand side of Eq. 31 corresponds to the momentum fraction of the target carried by the quark q while the second term was shown to encode information about the spatial distribution of forces experienced by quarks and gluons inside hadrons [11]. Consequently, measuring the ξ-dependence of GPDs is providing an alternative access to the strong force distribution and would also provides a deeper investigation of the ξ-independence of the Ji sum rule.

3.4 Note on additions to the J/Ψ program from our experiment

Besides "doubling the statistics" in certain regions of the approved J/Ψ measurement done in parallel to ours, which present some interests but doesn't add to the physics case (furthermore, the muon detector acceptance is limited), we would like to mention an extra-motivation in analysing the muon channel in parallel to the electron one, enabled by the additional muon detector for J/Ψ data interpretation.

Besides a small kinematic term difference, J/Ψ data in the e^+e^- and the $\mu^+\mu^-$ decay channels, in the same kinematic range, are expected to give the same cross sections. This is assuming a significant momentum gap between the pair's electron and the beam one, allowing to "distinguish" theoretically identical

lepton for virtual photon's kinematics experimental reconstruction purpose. We are interested in knowing the limits of this approximation for experiments where we are measuring 2 identical leptons in the final state. Observed differences between the e^+e^- and the $\mu^+\mu^-$ may help us to assess what would be the minimal energy-momentum gap between the electrons to rely on this approximation.

Furthermore, we will learn from experimental results about the limitations for muon's reconstruction in the general SoLID spectrometer, without a dedicated muon detector, compared to resolutions from our results with the muon detector.

3.5 Summary of our physics motivations

Our main goal is to provide constraints on the GPD H of the proton in the ERBL region from the extraction of the DDVCS+BH CFFs at various ξ and ξ' kinematics. It will be done from fitting of the beam spin asymmetry of DDVCS+BH at several t, ξ and ξ' points. It will be the first GPD sensitive measurement in this region and enable the deconvolution of the kinematics x and ξ, essential for tomographic interpretations of the GPDs via momentum dependent impact parameter parton distribution functions. We aim at extracing CFFs for the kinematics of our experiment, from beam spin asymmetries, to complement GPD models and bring constraints on the ξ dependence of the GPDs.

4 Experimental Setup

4.1 SoLID DDVCS Setup

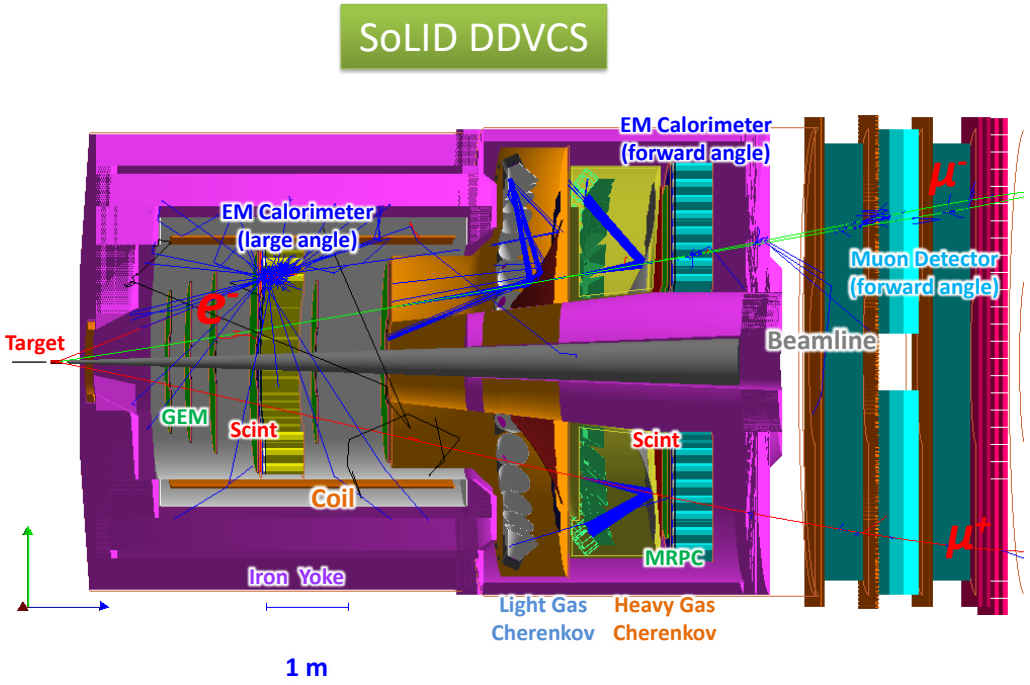

Figure 14: SoLID DDVCS with the forward angle muon detector added to the $J\psi$ setup, in Geant4 simulation.

SoLID DDVCS setup is shown in Fig. 14. It is based on the $J\psi$ setup with forward muon detector added. SoLID will be an all-new detector in Hall A during the 12 GeV era [62]. It is designed to use a solenoid field to sweep away low-energy charged background particles, and can thus carry out experiments using high-energy electron beams incident on unpolarized or polarized targets at luminosities up to $L = 10^{37}$ cm^{-2} sec^{-1} in an open geometry. It has two groups of the detectors. The forward-angle detectors cover polar angle from 8.5° to 16° and consist of several planes of Gas Electron Multipliers (GEM) for tracking, a light-gas Cherenkov (LGCC) for e/π separation, a heavy gas Cherenkov (HGCC) for π/K separation, a Multi-gap Resistive Plate Chamber (MRPC) for time-of-flight, and an Electromagnetic Calorimeter (FAEC). The large-angle detectors covers polar angle from 17° to 24.5° and consist of several planes of GEM for tracking, and an Electromagnetic Calorimeter (LAEC). Particles in SoLID will be detected and identified by measuring their momenta, time-of-flight, number of photons produced in the threshold Cherenkov counters, and energy losses in the calorimeters and MRPC.

The SoLID solenoid will reuse the CLEO-II magnet. Its superconducting coil and cryo will remain the unchanged. It has a large inner space with a clear bore diameter of 2.9 m and a coil of 3.1 m diameter. The coil length is 3.5 m, with a 3.8 m long cryostat. The coil is made of 5×16 mm^2 aluminum-stabilized superconductor, and runs at 3300 A. Part of the CLEO-II iron flux return will be modified and reused, and two new iron endcaps will be added at the front and back of the solenoid. The axial central field of the solenoidal magnet can reach about 1.4 T.

Six layers of GEM detectors will be used for tracking, providing information on the momentum, angle, and interaction vertex of the detected particles. They will be placed uniformly inside the solenoid magnet. For the forward angle detectors, five layers except for the first layer of GEM detectors will be used. In principle, three points are needed to reconstruct the kinematic variables. The fourth and fifth points will bring enough redundancy to compensate for the inefficiency of the GEM tracking detector. For the large-angle detectors, four layers of GEMs detector except the last two layers will be used. In this case, four layers are enough since the background level at large angles is expected to be smaller. SoLID GEMs will provide full azimuthal angular coverage by using trapezoidal-shaped sectors. The area of a single sector can be as large as 100 cm $\times$ 40 cm. Recent advancements in technology, like single-mask GEM etching and GEM splicing, makes it possible to fabricate GEM foils up to 100 cm $\times$ 200 cm. The GEM readout is by 2D strips readout by VMM chips developed for ATLAS Small Wheel Micromegas detectors.

The Cherenkov detectors at forward angles have two parts. The light-gas one uses a standard CO_2 gas radiator and can provide e/π separation up to momenta of 4.9 GeV/c with pion rejection in order of 10^3. The heavy-gas one uses C_4F_8 gas at 1.7 atm and gives a momentum threshold of 2.5 GeV/c and 7.5 GeV/c for pions and kaons, respectively. In both cases, the Cherenkov light is directed by the mirror systems onto Multi-Anode PMTs (MAPMTs) for readout.

There is one electromagnetic calorimeter at forward angles and one at large angles. They are made with identical Shashlyk-type modules. Each module is made of a pre-shower and a shower part. The pre-shower detector is simply a 2 radiation-length lead layer and a 2 cm thick scintillator with embedded wave-length-shifting (WLS) fibers for readout. The shower detector is of Shashlyk type, consisting of about 200 layers of 0.5 mm lead and 1.5 mm scintillator, and many WLS fibers penetrating all layers with a density about $1/\text{cm}^2$ for readout at the back of a module. This type of design can reach a pion rejection factor of more than 100, with good electron efficiency. Its radiation hardness is in the order of 500 krad, which satisfies the high-luminosity condition in SoLID.

MRPC-based time-of-flight systems have recently been used in the RHIC STAR and LHC ALICE experiments, providing a typical time resolution close to 100 ps. With readout strips, it can work inside a magnetic field. Using low-resistive glass, it can gain even an higher rate capability. SoLID experiments have a forward-angle MRPC as part of the planned baseline equipment.

Scintillator pad detector (SPD) will placed at both forward and large angle. FASPD will provide combined photon rejection with MRPC, but TOF will rely on MRPC for its better time resolution of 100 ps. LASPD will provide both photon rejection and TOF with time resolution of 150 ps.

4.2 Muon Detector

The experiment E12-12-006 was approved to measure J/Psi (E12-12-006) near Threshold Electrproduction of J/Psi at 11 GeV. We are proposing to supplement the J/Psi setup with a new forward angle muon detector to take parasitic data in parallel with the J/Psi experiment.

For the muon detector, we will be reusing the additional iron plates from the CLEO II magnet. Only two inner layers are planned to be used for the SoLID detector. The third and outer layer of iron is made of 8 iron plates about 533 cm long and will not be used for SoLID magnet. We will reuse the 6 of 7 available plates for the muon detector. We are planning to lay the iron in 3 layers with a layer of straw tubes between each. Two layer of XY scintillator planes will be included after the third iron layer serve as muon trigger as show in Figure 15. There is no known conflict in term of space and engineering concern for the planned muon detector location. A preliminary concept design by Orsay engineer of holder for the iron plates is also shown in Figure 16. A TOSCA field calculation has shown the solenoid field has almost no effect on those iron plates with the forces of order one Newton and torques of order 2 N-m.

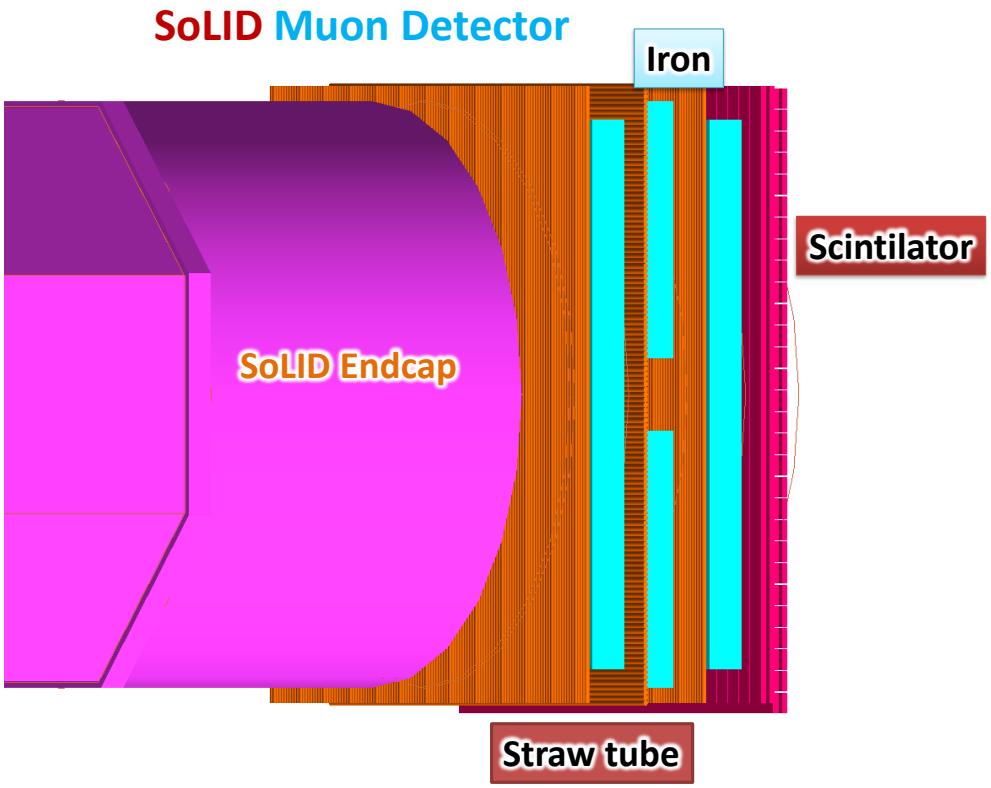

Figure 15: Preliminary design of SoLID muon detector at forward angle in Geant4 simulation.

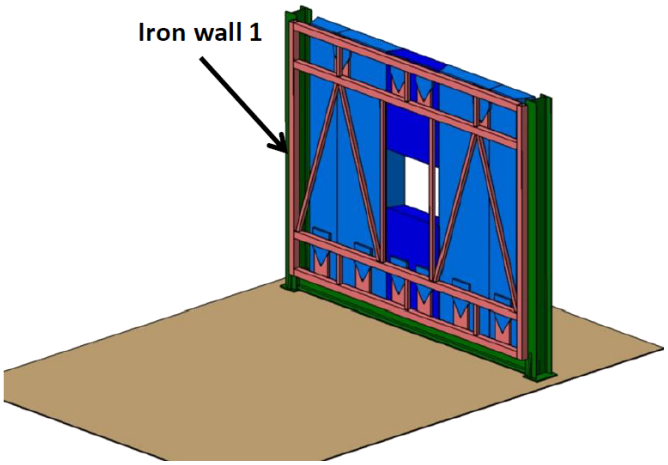

Figure 16: Preliminary design by Orsay engineer of holder for the iron plates

4.3 Data acquisition

The GEM readout was initially designed to use the APV25 for the readout but is switching to VMM3 readout. The VMM3 chip is a 64 channels ASIC providing time and amplitude for each channel, a prototype for SoLID GEM readout was developed to be able to handle up to 10 MHz per channel.

Most photosensors are readout using JLab FADC 250 MHz which are 16 channels VME board sitting in a VXS crate. The VXS backplane has 4 point to point high speed serial connection up to 5 Gbps, this allows to create a trigger based on FADC data. One unused lane from FADC was used for Fast Readout of FADC, increasing the data rate from about 100 MB/s to 500 MB/s, effectively increasing the bandwidth by a factor 80 since boards can be read out in parallel. This allows to transfer the FADC data at higher rate to reach a trigger rate of 200 KHz, as the baseline maximum rate for the experiment.

Since muons leave low energy in the calorimeter, a dedicated muon triggers has to be developed based on the muon detectors located after the calorimeter. Indeed since muons are heavy leptons they radiate much less than electrons and can get through large amount of materials. The signal for triggering will be provided by muon trigger scintillator plane signals that will be further fed into a JLab custom logic module. It is a 250 MHz pipeline module able to built coincidence every 4 ns at 1 ns resolution. The trigger will search for coincidence between several layers of trackers looking for zone of interest and clean tracks. The muon trigger will look for the coincidence of two candidate muon tracks to reduce the effect of single pion/muon background. The main trigger will be a coincidence between the standard calorimeter trigger and the muon detector. Additional lower level triggers would also be implemented for a precise understanding of the detectors acceptances and efficiencies.

The J/Psi experiment triggers are positron and electron in calorimeter and light gas Cerenkov for photoproduction with about 60 kHz trigger rate. To run DDVCS in parallel, an additional dimuon trigger will be set up. Singles rate in muon detector is mostly dominated by pion and muon from pion decay. Rates were about 35 KHz for each polarity, giving a 70 KHz total single rates. Assuming a 50 ns coincidence window this gives about 0.25 KHz dimuon trigger rate. Total expected trigger rate is thus about 61 KHz, which is well within the DAQ capabilities of 200 KHz.

5 Simulation and Projection

The Geant4 simulation was conducted using the program "solid_gemc" with full SoLID DDVCS setup including all subsystems and materials. And the projections are made based on GPD model with statistic error from Geant4 simulation.

5.1 Acceptance and efficiency

We plan to detect the scattered electrons and decay muons to reconstruct the DDVCS reaction. Single particle acceptance for both electron and muon are studied by throwing them evenly into the setup from the target location with vertex covering the full target length. The expected acceptance in polar angle and momentum is shown on Fig. 17. The low momentum cut off for electrons is mostly from magnetic field and SoLID forward angle boundary, while the low momentum cut off for muon near 2 GeV is mainly from materials blocking. Both geometry and decay effect are included in this study. However to count for PID and tracking efficiency, we estimate the total muon efficiency about 87% and total electron efficiency about 90%. The total efficiency for one electron and two muons thus is about 70%. Some of recoil protons could be also be detected by time of flight detector and tracking and they will provide some cleaning data samples with lower statistics.

5.2 Physics coverage

Since the DDVCS event will not be measured separately but in combination with the Bethe-Heitler (BH) events with much large cross section, the physics rate estimation is simple based on the BH event generator "grape-dilepton" [63]. The program is widely used for various studies for ep collisions and its cross section calculation is based on exact matrix element in the electroweak theory at tree level. The results for 3-fold coincidence with proton missing is shown in Figure 18 and Figure 19.

Using the J/Ψ experiment luminosity and running time, it was determined that the total number of muons pairs of BH events has following the distributions shown in 20. There are about 30k events between 2 and 3 GeV of the resonance free region, 600k events between 1 and 3 GeV, and 800k events in total. A factorization cut like $-t < Q^2$ would only cut away about 10% of events. With such high statistics, we can afford to bin data into almost 500 of 5D kinematic bins of 1000 events to measure asymmetry and fit to GPD models.

5.3 Event identification and exclusivity

The main handle on exclusivity is through the missing mass of $(e\mu^+\mu^- X)$, where X will be at the proton mass for exclusive events. The SoLID tracking resolution was evaluated using the electron and proton momentum tracking resolution for the J/Psi experiment for the proton which will be worse than for muons. We have added an additional 1.5 safety factor on all tracking resolution. Figure21 shows that SoLID tracking resolution is sufficient to have a clean sample of exclusive event by putting a cut at the one pion threshold.

5.4 Background

Extensive background studies were carried out for the J/Psi experiment and showed that SoLID could handle a luminosity of 10^{37} and the luminosity was chosen for optimal reconstruction of J/Psi events. The background for DDVCS inside of SoLID will be similar to the J/Psi experiment.

Our background study focus on the background in the muon detector using full Geant4 simulation and physics generators. The beam induced low energy background were evaluated with 11GeV electron beam shooting on the 15 cm long liquid hydrogen target and they are mostly contained within SoLID endcap and has negligible effect in the muon detector.

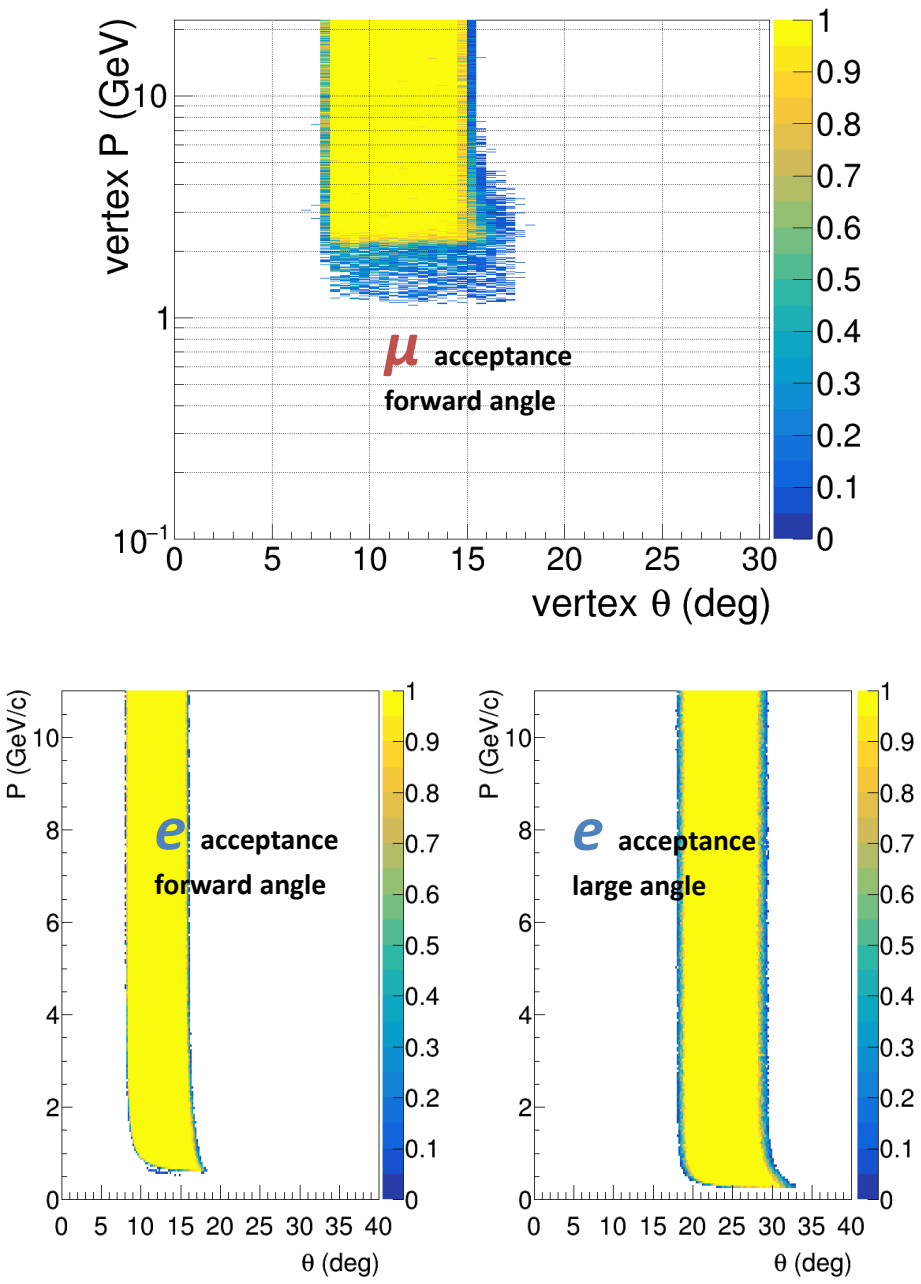

Figure 17: The acceptance for μ (top) and e (bottom) at the SoLID forward angle and large angle detectors.

The main background for measurement is from pion which could be easily misidentified as muons. The main muon identification/pion rejection is given by the layers of iron, pion are more likely to interact with material through hadronic process than muons. Once a pion decay into a muon, the muon detector can't distinguish it from the DDVCS muon any more. But the tracking detector can still help reject those decay muon by performing vertex cut, even though not at trigger level.

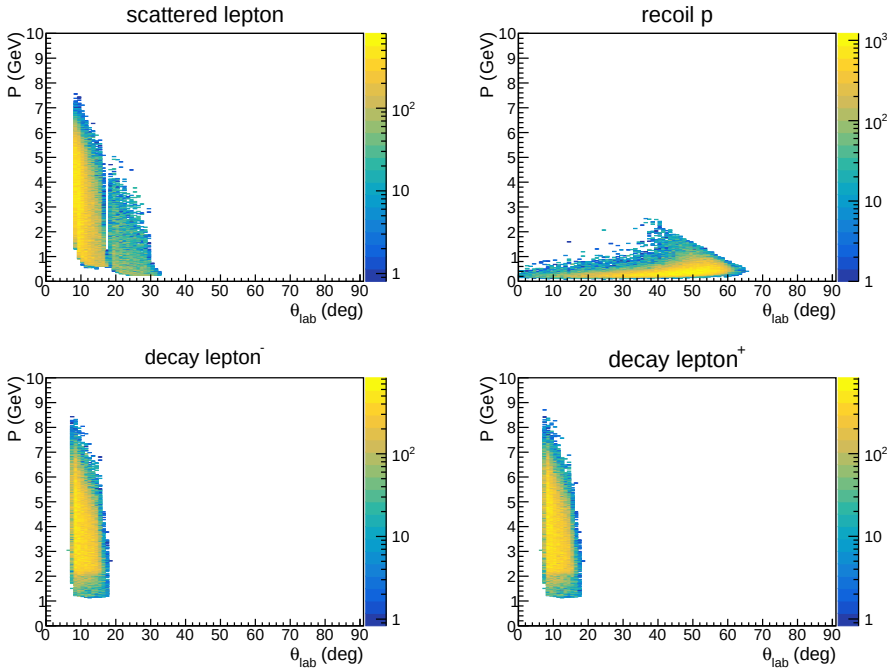

Figure 18: Momentum and angular distribution of BH events

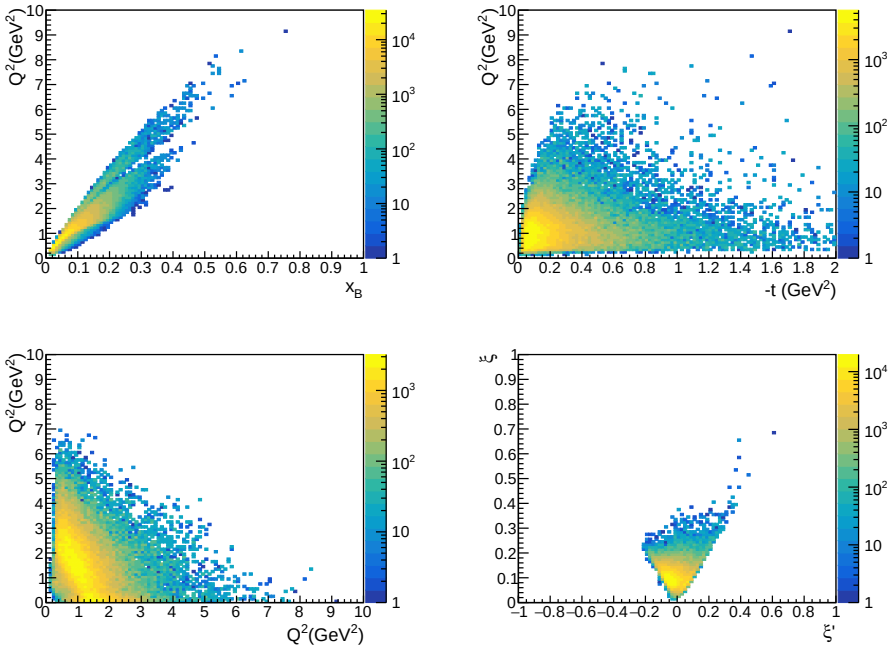

Figure 19: The SoLID detector with $J\psi$ setup in Hall A.

5.4.1 Single pion background

The single pion background rate was evaluated by using the "evgen_bggen" event generator which combines PYTHIA event generator with resonance model from both electroproduction and photoproduction. The

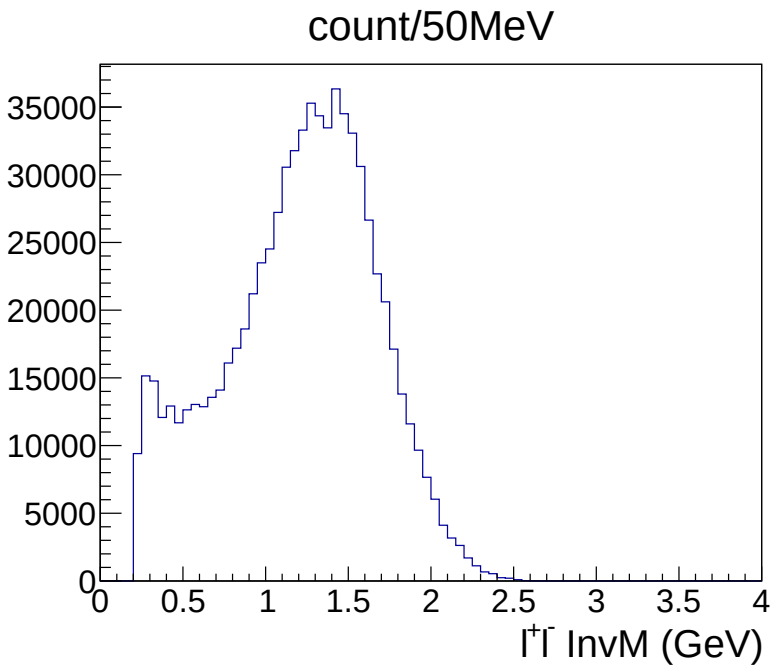

Figure 20: Total expected BH muons pairs detected for the run time

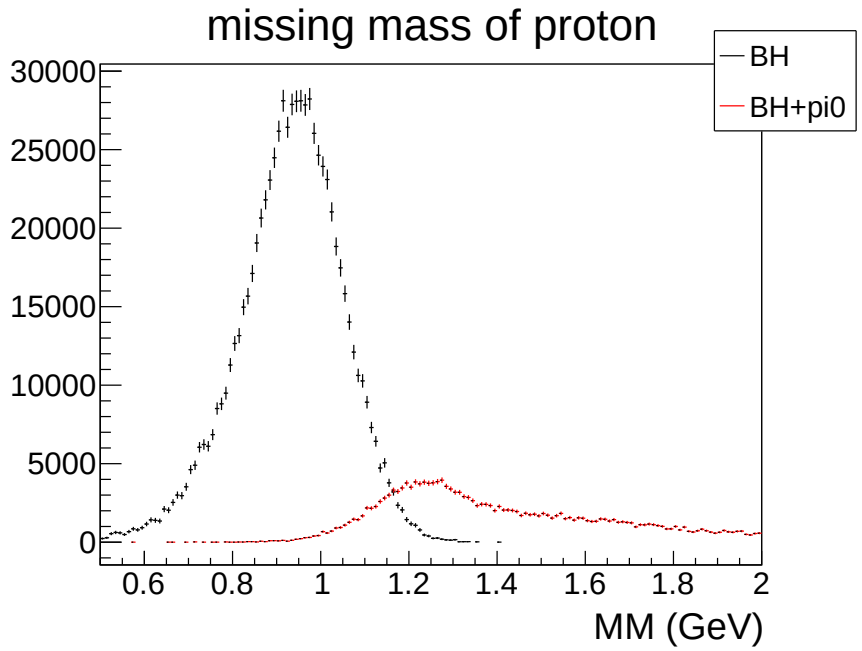

Figure 21: Missing mass distribution for exclusive BH events in black and the BH events with one additional neutral pion in red.

SoLID DDVCS Geant4 simulation including all materials are used to model pion blocking and its muon decay. The surviving probability of primary and secondary pions and their decay muons at the scintillator planes of the forward angle muon detector are shown in Fig. 22. The primary pions from the target can have 0.1% chance to survive, while secondary pions produced by primary pions along the way can have a couple

percent. Muons from primary pion decay have the probability of decaying and reaching the detector from 0.1% to 1%.

Combining the two together, we obtained and single pion and muon rate at the back of the forward muon detector after 3 layers of iron. Their rate distribution over polar angle and momentum are shown in Figure 23. The total rate of negative pion is 9 khz and negative muon is 26 khz. The positive pion and muon have similar rate. So the total rate is about 70khz. We do not expect any issues operating the straw tube chamber which could handle 1 MHz of rate for the Seaquest experiment [58]. The coincidence trigger rate requiring two charge particles at the back of the muon detector is about 0.25 kHz, assuming 50 ns coincidence timing window.

For offline analysis, the timing and vertex coincidence of three particles of electron and muon pair are required. There could be accidental background from an event of electron and pion (dominant by SIDIS process) about 100 Hz and a separate single pion event about 35 khz. A timing coincidence of those two background within 50 ns can have the rate about 0.18 hz which is the same level of BH event rate. Further vertex coincidence and vertex cut of decaying muon from pion can reduce the background rate to 10% and less comparing of the physics events.

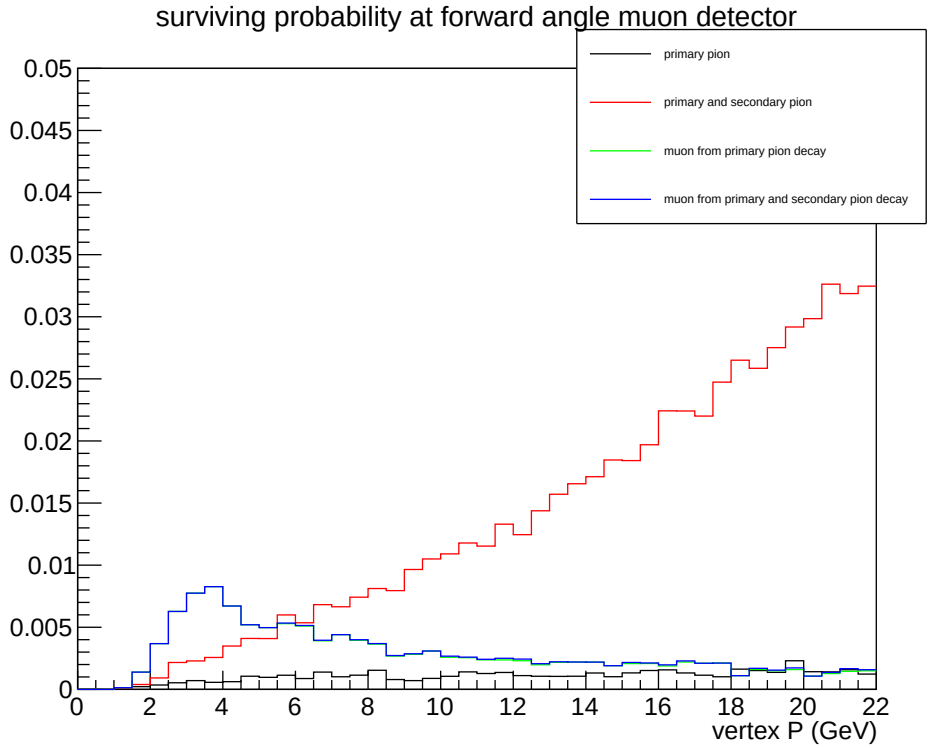

Figure 22: The surviving probability of primary and secondary pions and their decay muons at the scintillator planes of the forward angle muon detector. The primary pions from the target can have 0.1% chance to survive, while secondary pions produced by primary pions along the way can have a couple percent. Muons from primary pion decay have the probability of decaying and reaching the detector from 0.1% to 1%.

5.4.2 Two pion exclusive background

Another background important for the offline analysis is the two pion exclusive channels. It will pass the two charge particle coincidence trigger in the muon detector and most likely survive the missing proton

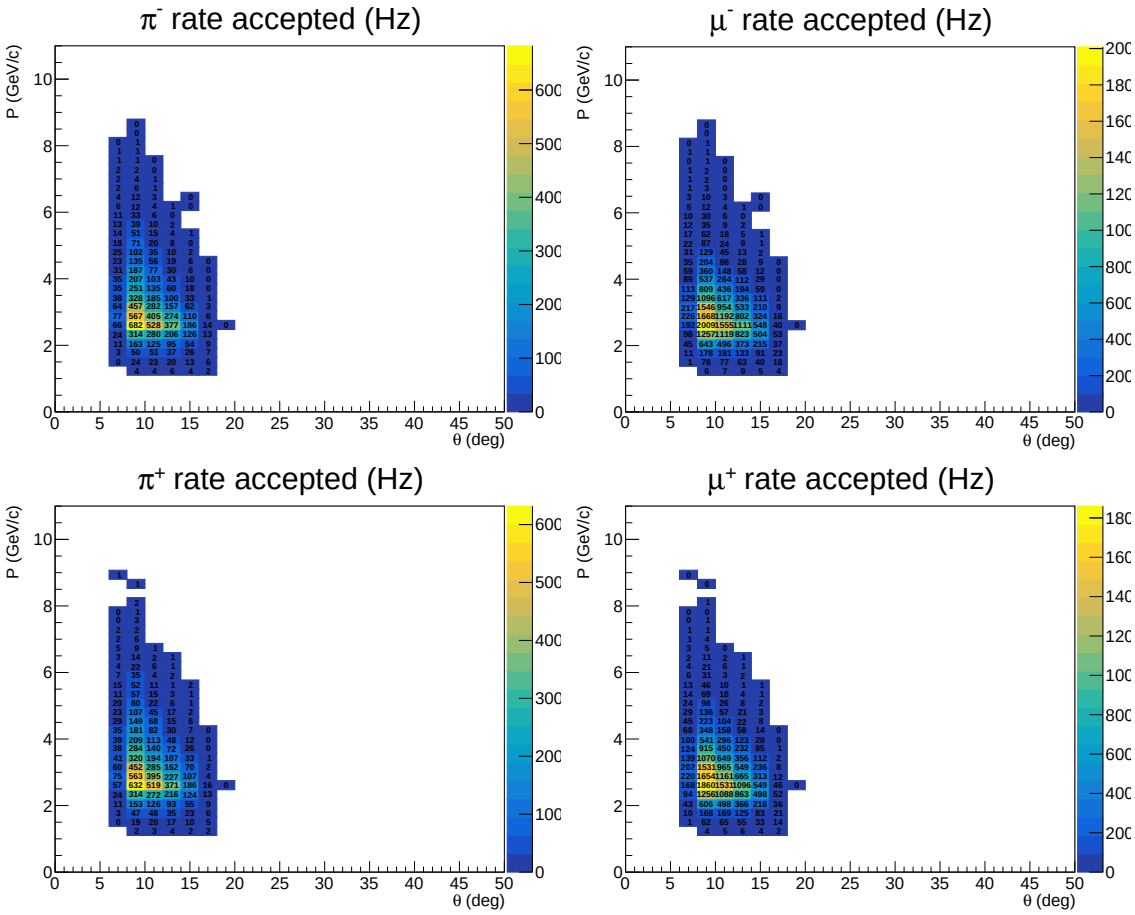

Figure 23: Single particles rate of pion and muon from pion decay at the back of forward angle muon detector. They include both pions directly from target and all secondaries and muons from their decay.

mass exclusivity cut because muon and pion mass are close. We used the event generator "twopeg" [64] to study the channel $\vec{e}p \to ep\gamma^* \to ep\pi^+\pi^-$. It includes both resonance and non-resonance regions and fits the five-fold differential structure functions from the recent versions of the JM model to all results on charged double pion photo- and electroproduction cross sections from CLAS 6GeV. To estimate the cross sections in the regions not covered by data, a specialized extrapolation is used to extend the coverage to 12 GeV beam to cover in W from the reaction threshold up to 4.5 GeV. We expect the code will be developed further once CLAS12 results are finalized. But its current results should be reliable enough as it was used in CLAS12 analysis and proposals.

Combining the "twopeg" generator and SoLID DDVCS Geant4 simulation, we obtained the counts from the two pion exclusive channels as shown in Figure 24. The results are separated into the cases for neither pion decays, negative pion decays into muon, positive pion decays into muon, and both pions decay. The first 3 cases have small counts because of the strong pion blocking. The last case have counts about 10% of the BH muon counts. Tracking with vertex cuts will further reduce it to a couple percent level, comparing to BH counts shown in Figure 20.

5.5 Expected results

We used several event generators for our projections: Grape [63] (used for acceptance), DEEPGen [65] (mainly for theoretical projections and counting rates) and "Orsay" (checking counting rates). This particu-

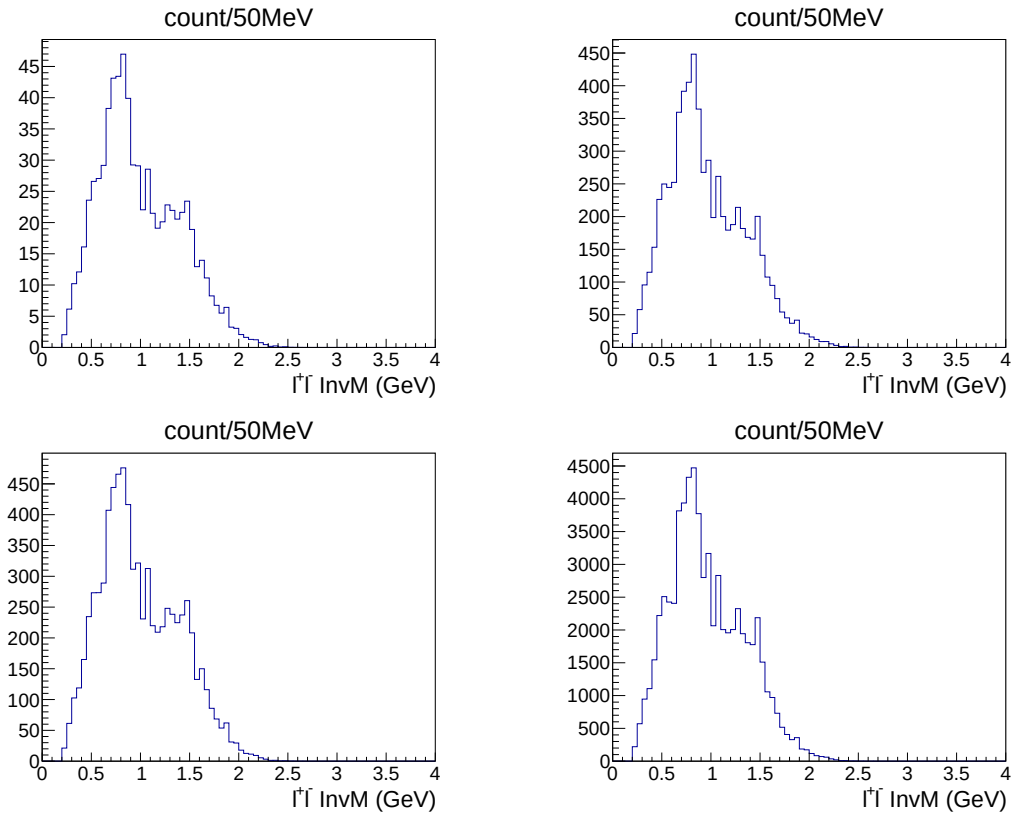

Figure 24: From left to right and top to bottom, the counts from the two pion exclusive channel contamination are shown in 4 cases, neither pion decay, negative pion decays into muon, positive pion decays into muon, and both pions decay.

lar generator is based on the H-only VGG model [19] at leading-twist, and extended to include the $\{E, \widetilde{H}, \widetilde{E}\}$ GPDs of the nucleon [60], has been developed to evaluate projected data of the SoLID DDVCS experiment. The twist-3 $d^5\widetilde{\sigma}_{DDVCS}$ contribution to the $eN\mu^+\mu^-$ polarized cross section currently vanishes in this approach further detailed in Ref. [61]. In [65], we used the more conservative approach to only including the GPD H due to differences in models for GPD E projections. Grape [63] has been used by many collaborations.

For the detection of the scattered electrons and the produced muon-pairs, the SoLID DDVCS acceptance is considered and an overall 70% detector efficiency is taken into account to obtain the $eN\mu^+\mu^-$ event counts for the data taking scenario previously described.

The distribution of the projected count number in the $(Q^2, -t)$ and (ξ', ξ) physics phase-spaces are shown in Fig. 19. The experiment covers a broad kinematic range limited on the one hand by the condition -$t \ll Q^2$ required for the factorization of hard and soft scale physics of the process, and on the other hand by the TCS and the DVCS correlation lines. With high statistics, the DDVCS reaction can be studied in all 5 kinematic variables $(\xi', \xi, Q^2, t, \phi)$ independently. The full set of cross section and asymmetry observables can be measured over these phase-spaces, allowing to constrain GPDs in uncharted territories. The example of the ϕ-distributions of projected data are shown in Fig. 25 for the BSA measured with a polarized electron beam. Two different (ξ', ξ, Q^2, t) kinematics are chosen to illustrate the experimental exploration of the sign change of the BSA as ξ' cross over from negative to positive values. The expected experimental signals are of significant amplitudes, enabling a meaningful extraction of the CFFs from the ϕ-modulation of observables over the broad kinematic domain of the experiment. These data will provide invaluable constraints for a coherent determination of GPDs through global fit methods.

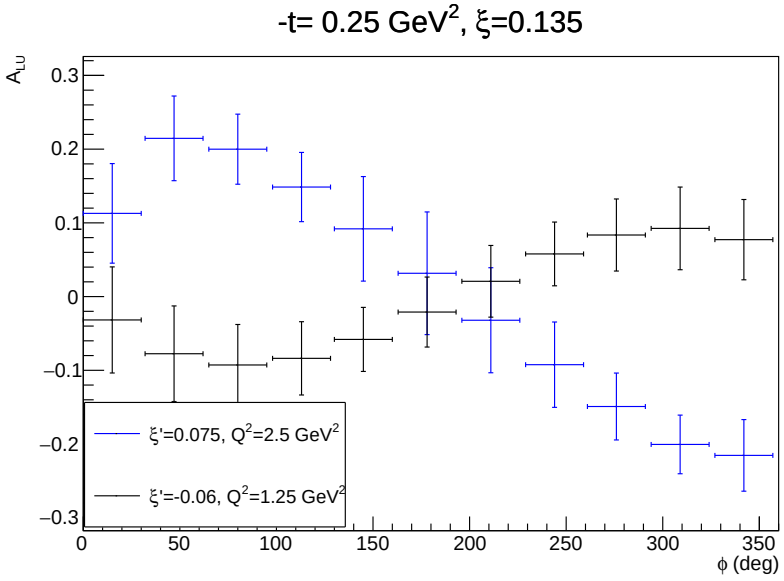

Figure 25: Example of asymmetry as a function of ϕ angle for a bin centered at ξ=0.135 and t = -0.25 GeV^2 for two values of Q'^2 and ξ', one can notice the sign change of asymmetry when ξ' changes from negative to positive.

6 Beam time request

The proposed experiment is just adding the muon detector and will run concurrently with the SoLID J/Psi experiment (E12-12-006)'s approved 60 days and is not requesting any additional beam time.

This setup will also complement the statistics of the J/Ψ experiment by detecting the muon channel at the same time. The luminosity during the experiment is planned to be $10^{37}.cm^{-2}.s^{-1}$., depending on the background in the detector the luminosity might be increased to obtain more data.

7 Responsibilities

The muon detectors will be joint responsibility between Rutgers University for the Straw Tube Chambers and Virginia Tech for the scintillator trigger planes and readout electronics. JLab and Orsay will collaborate on mechanical design for the muon detectors. JLab will be in charge of integrating the muon detector into the SoLID DAQ. Duke University will work on simulation and PID algorithm.

8 Conclusion

We are proposing to complement the SoLID J/Psi setup with a new forward angle muon detector. This would allow a first DDVCS measurement in the dimuon channel while also increasing the statistics of the J/Ψ experiment. The measured quantity

$$\begin{aligned}\left\{ \begin{array}{c} A_{\rm LU}^{\sin\phi} \\ A_{\rm LU}^{\sin\varphi_\mu} \end{array} \right\} &= \frac{1}{\mathcal{N}} \int_{\pi/4}^{3\pi/4} d\theta_\mu \int_0^{2\pi} d\varphi_\mu \int_0^{2\pi} d\phi \left\{ \begin{array}{c} 2\sin\phi \\ 2\sin\varphi_\mu \end{array} \right\} \frac{d^7\overrightarrow{\sigma} - d^7\overleftarrow{\sigma}}{dx_B\, dy\, dt\, d\phi\, dQ'^2\, d\Omega_\mu} \\ &\propto \Im\mathrm{m}\left\{ F_1\mathcal{H} - \frac{t}{4M_N^2} F_2\mathcal{E} + \xi'(F_1+F_2)\widetilde{\mathcal{H}} \right\}, \end{aligned} \tag{32}$$

will give access to the imaginary part of a linear combination of Compton Form Factors, at values of $\xi' \neq \xi$.

The ξ dependence of GPDs is particularly useful to determine the constant term of the GPDs which can be related to mechanical properties of the nucleons. This measurement will pave the way of future measurements DDVCS measuremts to map out GPDs out-of the diagonal regions, opening access to a fully experimental determination of parton transverse densities.

This experiment and the observable (DDVCS beam spin asymmetry) is unique both with regards to what is going to be measured as well as its physics outcome and will have a major impact for tomographic interpretations of the nucleon structure by bringing experimental constraints on GPDs ξ dependencies and kinematical variable deconvolution, and their extrapolation to zero skewness.

References

[1] A. V. Belitsky, D. Müller, Phys. Rev. D **68**, 116005 (2003).

[2] I.V. Anikin et al., Acta Physica Polonica 49 (2018) 741

[3] K. Deja, V. Martinez-Fernandez, B. Pire, P. Sznajder, J. Wagner, arXiv:2303.13668 [hep-ph] - accepted in Phys. Rev. D (2023)

[4] K. Deja, V. Martinez-Fernandez, B. Pire, P. Sznajder, J. Wagner, arXiv:2304.03704 [hep-ph]

[5] D. Müller, D. Robaschick, B. Geyer, F.M. Dittes, J. Hořejši, Fortschr. Phys. **42**, 101 (1994).

[6] X. Ji, Phys. Rev. Lett. **78**, 610 (1997).

[7] A.V. Radyushkin, Phys. Rev. **D 56**, 5524 (1997).

[8] M. Diehl, Phys. Rep. **388**, 41 (2003).

[9] A. V. Belitsky, A. V. Radyushkin, Phys. Rept. **418**, 1 (2005).

[10] X. -D. Ji, Phys. Rev. D **55**, 7114 (1997).

[11] M. Polyakov, Phys. Lett. B **555**, 57 (2003).

[12] J. C. Collins and A. Freund, Proof of factorization for deeply virtual Compton scattering in QCD, Phys. Rev. D 59 (1999) 074009.

[13] M. Burkardt, Phys. Rev. D **62**, 071503(R) (2000).

[14] J.P. Ralston, B. Pire, Phys. Rev. D **66**, 111501(R) (2002).

[15] M. Diehl, Eur. Phys. Jour. C **25**, 223 (2002).

[16] A.V. Belitsky, D. Müller, Nucl. Phys. A **711** (2002) 118c.

[17] A.V. Belitsky, D. Müller, A. Kirchner, Nucl. Phys. B **629**, 323 (2002).

[18] P. Chatagnon et al. (CLAS Collaboration) Phys. Rev. Lett. 127, 262501

[19] M. Guidal, M. Vanderhaeghen, Phys. Rev. Lett. **90**, 012001 (2003).

[20] A. V. Belitsky, D. Müller, Phys. Rev. Lett. **90**, 022001 (2003).

[21] A. Luboz, internship report (2015).

[22] M. Vanderhaeghen, P.A.M. Guichon, M. Guidal, Phys. Rev. D **60**, 094017 (1999).

[23] (Hall A DVCS Collaboration) C. Muñoz Camacho *et al.*, Phys. Rev. Lett. **97**, 262002 (2006).

[24] (H1 Collaboration) C. Adloff *et al.*, Phys. Lett. B **517**, 47 (2001).

[25] (ZEUS Collaboration) S. Chekanov *et al.*, Phys. Lett. B **573**, 46 (2003).

[26] (CLAS Collaboration) H.S. Jo *et al.*, Phys. Rev. Lett. 115, 212003 (2015).

[27] (Hall A DVCS Collaboration) M. Defurne *et al.*, (Jefferson Lab Hall A), Phys. Rev. C 92 (2015) no.5

[28] F. Georges et al. (Jefferson Lab Hall A Collaboration) Phys. Rev. Lett. 128, 252002

[29] N. Hirlinger Saylor et al. (CLAS Collaboration), Phys. Rev. C 98, 045203 (2018).

[30] R. Akhunzyanov et al., (COMPASS Collaboration), Phys. Lett. B 793 (2019) 188. (Erratum: Phys.Lett.B 800, 135129 (2020)).

[31] M. Benali et al., Nat. Phys. 16, 191 (2020)

[32] (Hall A DVCS Collaboration) M. Mazouz *et al.*, Phys. Rev. Lett. **99**, 242501 (2007).

[33] (HERMES Collaboration) A. Airapetian *et al.*, Phys. Rev. Lett. **87**, 182001 (2001).

[34] (CLAS Collaboration) S. Stepanyan *et al.*, Phys. Rev. Lett. **87**, 182002 (2001).

[35] (CLAS Collaboration) F.X. Girod *et al.*, Phys. Rev. Lett. **100**, 162002 (2008).

[36] (CLAS Collaboration) S. Chen *et al.*, Phys. Rev. Lett. **97**, 072002 (2006).

[37] (HERMES Collaboration) A. Airapetian *et al.*, JHEP **06**, 019 (2010).

[38] (CLAS Collaboration) E. Seder *et al.*, Phys. Rev. Lett. **114**, 032001 (2015).

[39] (CLAS Collaboration) S. Pisano *et al.*, Phys. Rev. D **91**, 052014 (2015).

[40] (HERMES Collaboration) A. Airapetian *et al.*, Phys. Lett. B **704**, 15 (2011).

[41] (HERMES Collaboration) A. Airapetian *et al.*, Phys. Rev. D **75**, 011103 (2007).

[42] (HERMES Collaboration) A. Airapetian *et al.*, JHEP **06**, 066 (2008).

[43] M. Boer, Doctorat Thesis, Université Paris Sud, IPNO **T-14-05**, (2014).

[44] E. Voutier, *Nuclear Theory*, Edts. A. Georgieva and N. Minkov, Heron Press, **33**, 142 (2014).

[45] P. Hoodbhoy, X. Ji, Phys. Rev. D **58**, 054006 (1998).

[46] M. Burkardt, Int. J. Mod. Phys. A **18**, 173 (2003).

[47] Huey-Wen Lin Phys. Rev. Lett. 127, 182001 (2021)

[48] K. Goeke, M.V. Polyakov, M. Vanderhaeghen, Prog. Part. Nucl. Phys. **47**, 401 (2001).

[49] Y. Kubota *et al.*, Nucl. Inst. Meth. A **320**, 66 (1992).

[50] P. Souder, JLab Proposal **E12-10-007** (2010).

[51] J.P. Chen, H. Gao, X. Jiang, J.C. Peng, X. Qian, JLab Proposal **E12-10-006** (2010).

[52] J.P. Chen, Y. Qiang, W. Yan, JLab Proposal **E12-11-007** (2011).

[53] K. Allada, J.P. Chen, H. Gao, Z.E. Meziani, JLab Proposal **E12-11-108** (2011).

[54] K. Hafidi, X. Qian, Z.E. Meziani, N. Sparveris, Z. Zhao, JLab Proposal **E12-12-006** (2012).

[55] K. Gnanvo *et al.*, Nucl. Inst. Meth. A **782**, 77 (2015).

[56] C. Altunba *et al.*, Nucl. Inst. Meth. A **490**, 177 (2002).

[57] B. Ketzer *et al.*, Nucl. Inst. Meth. A **535**, 314 (2004).

[58] C. A. Aidala *et al.* [SeaQuest], Nucl. Instrum. Meth. A **930**, 49-63 (2019) doi:10.1016/j.nima.2019.03.039 [arXiv:1706.09990 [physics.ins-det]].

[59] C. L. Morris *et al.* (2008) Tomographic Imaging with Cosmic Ray Muons, Science & Global Security, 16:1-2, 37-53]

[60] S. Zhao, PoS SPIN2018, 068 (2019). DOI 10.22323/1. 346.0068

[61] S. Zhao, Studying the nucleon structure via Double Deeply Virtual Compton Scattering at the Jefferson Laboratory. Ph.D. thesis, University Paris Saclay, Orsay

[62] SoLID Pre-Conceptual Design Report https://solid.jlab.org/DocDB/0002/000282/001/solid-precdr-2019Nov.pdf

[63] Computer Physics Communications 136, 126-147 (2001), https://research.kek.jp/people/tabe/grape

[64] CLAS12-NOTE-2017-001 (arXiv:1703.08081) and CLAS12-NOTE-2017-014 (arXiv:1712.07712), https://github.com/skorodumina/twopeg

[65] M. Boer, DEEPGen generator, Hall C public note 1000 (2019)